

# Response letter for the manuscript: Does the rotational direction of a wind turbine impact the wake in a stably stratified atmospheric boundary layer?

Comments to the Author:

Dear Authors,

As you can see, both reviewers remain very critical of your paper, and expressed the feeling that you were only superficially responding to their concerns. I believe that Reviewer 1 is raising serious concerns regarding your inflow profiles (e.g. Eq 4 and 5 do not correspond to the analytical model proposed by Shapiro & Fedorovich), and also the turbulence generation method that you use can have a significant influence on conclusions. You solve this by improving your boundary conditions and/or by providing evidence (with experimental data, as reviewer 2 suggest), that your results make sense. Also the second comment by Reviewer 1 is to the point. The model that you propose in Section 4 looks very heuristic, and it is not clear why you do not build on existing wake models, etc. I would encourage you to very carefully consider the reviewers comments, as I believe these are make-or-break issues for this work.

Sincerely,

Johan Meyers

Dear Prof. Johan Meyers,

thank you for the time you have devoted to the thoughtful consideration of our manuscript. Following your comments and the reviewers, we carefully considered the criticism and the way that we presented this work. Our intent for the paper is to make people aware that a wind turbine's rotational direction has an impact on the wake under veering inflow. Due to the presentation of some matters in the previous manuscript version, there were a few misunderstandings. Therefore, we have implemented several changes in the manuscript:

- There was a misunderstanding with the 'Simplified Wake Model'. Reviewer 1 suggested a comparison to existing wake models, which make us realize that the name 'Simplified Wake Model' was a perhaps misleading choice. Sect. 4 in the previous version was not intended to be a new wake model, comparable to existing well defined ones. It is simply a device to help to explain why a significant difference in the meridional wake component occurs depending on the rotational direction of the rotor under

veering inflow conditions.

Therefore, in the revised version of the manuscript we have changed the description and included this presentation and discussion in a very simplified equation in Sect. 3 'Analysis of a rotating system under veering inflow'. We further simplified the rather complex equations in the old version of the manuscript, to one analytic equation (Eq. 17). There is no need to use existing wake models as proposed by the reviewer 1, as we are not proposing a model to be used for other purposes like wake steering, energy production estimates, etc. Rather, we present this discussion to highlight the interaction of two physical processes (wake rotation and inflow veer) only. We subsequently interpret our LES results in light of this model of the interaction of these two physical processes.

- Reviewer 1 was concerned about our turbulence generation method. Therefore we have reverted to using established and published wind and turbulence profiles from LES from a diurnal cycle. We extract non-veered inflow from evening boundary layer (EBL) and veered inflow from stable boundary layer (SBL) portions of published in Boundary-Layer Meteorology, editor Fedorovich (Englberger and Dörnbrack, 2018). We therefore no longer reply on artificial inflow profiles (Eq. 4, and 5 in the previous version). The non-veered EBL and the veered SBL wind-turbine simulations are performed for a clockwise (CCW), a counterclockwise (CW), and no (NR) rotor rotation. To further justify our inflow, we compare these inflow profiles resulting from the diurnal cycle simulation to profiles of the Ekman-spiral in the new Eq. 7 and 8. The results show good for a typical SBL value of the eddy viscosity coefficient  $\kappa = 0.05 \text{ m}^2 \text{ s}^{-1}$ .

These six simulations (SBL\_CR, SBL\_NR, SBL\_CCR, EBL\_CR, EBL\_NR, EBL\_CCR) replace the six existing ones (V\_CCW, V\_NR, V\_CW, NV\_CCW, NV\_NR, NV\_CW) in the previous manuscript version. They have very similar characteristics (wind profiles, potential temperature, turbulence intensity), resulting therefore in similar wake characteristics. Our primary conclusion from the original manuscript persists, that in veered flow, CW rotation and CCW rotation exhibit very different wake characteristics. These results are now presented in Sect. 4: 'A rotating wind-turbine rotor under veering inflow' (Note we changed from CCW (counterclockwise wake) to CR (clockwise rotor), as we think it is more intuitive to give the rotor rotation.) Further, the new SBL simulations apply veer limited to the lower rotor half with a larger directional shear in this region than the 'V' simulations in the previous version.)

- Reviewer 2 suggested that we include a qualitative investigation of  $u$  and turbulence intensity  $TI$ . This new discussion appears in Sect. 4 as well as in Figs. 11 and 12.
- A 'Comparison of a rotating wind turbine under veering inflow to analysis predictions' follows in Sect. 5. It interprets the results in Sect. 4 using the new simple analysis in Sect. 3. This new Section has the same intent as Sect. 4.2 in the previous version.
- Reviewer 2 further suggests a quantitative comparison to measurements. However, the LES result from an idealized diurnal cycle simulation. There-

fore, no measurements are available for exactly these conditions. However, in the text, we compare the wake structures (skewness under veering inflow etc.) to other studies, to show that the results are reasonable and consistent with previous work, and benefit from the explanation afforded by the simple analysis in the new Sect. 3. Further, the new set of simulations are based on previously published results and so should not incur any questions regarding the turbulence generation method.

- Despite these extensive changes to the simulations, the simple analysis, and the discussion of the results, the basic motivation of the paper is the same. Therefore, the introduction and conclusion have only minor changes.

In summary, we have put substantial effort into responding to the reviewers' comments and hope you find the manuscript suitable for publication. We have removed the reasons for reviewers' concerns with inflow by using established and published simulations. We have avoided the need for using existing wake models by instead presenting a simplified analytic model that focuses on the two main physical processes at play: inflow veer and wake rotation. Our fundamental point, that turbine rotation interacts with atmospheric profiles in interesting ways, should be much more clear now. The main results have not changed although the mechanism by which we calculated them has changed in response to reviewer suggestions.

Thank you for your consideration.

#### Reviewer 1: Mayor revisions

The authors did not address the main issues raised in the first review. Also, considering the new information provided in the revised manuscript, unfortunately, I cannot recommend the manuscript to be published. The major comments are:

We thank the reviewer for the time they devoted to considering our manuscript. We have made substancial changes based on their comments, and we hope the manuscript is now suitable for publication.

We carefully considered the criticism and the way that we presented this work. Our intent for the paper is to make people aware that a wind turbine's rotational direction has an impact on the wake under veering inflow. Therefore, we perform extensive changes to the simulations, the simple analysis, and the discussion of the results. Our primary conclusion from the original manuscript persists, that in veered flow, CW rotation and CCW rotation exhibit very different wake characteristics. As the basic motivation of the paper is the same, the introduction and conclusion have only minor changes.

#### Reviewers comments:

1. Regarding the Simulation: in the revised version and the response letter, the authors provided more details about the inflow conditions. The main issue with this study is that the inflow conditions for veering and non-veering cases are not physical. In other words, the inflow profiles for velocity and Reynolds-stresses for the veering inflow is not similar to (even) idealizes boundary layers with Coriolis effects. The authors can refer to the previous studies on this topic in which a precursor technique is used to generate appropriate inflow conditions for different veering scenarios (e.g., KU Leuven, NREL, EPFL, ...). As the inflow conditions are incorrect and non-physical, the rest of the analysis and the conclusions cannot be justified.

Reviewer 1 was concerned about our turbulence generation method. Therefore we have reverted to using established and published wind and turbulence profiles from LES from a diurnal cycle. We extract non-veered inflow from evening boundary layer (EBL) and veered inflow from stable boundary layer (SBL) portions of published in Boundary-Layer Meteorology, editor Fedorovich (Englberger and Dörnbrack, 2018). We therefore no longer reply on artificial inflow profiles (Eq. 4, and 5 in the previous version). The non-veered EBL and the veered SBL wind-turbine simulations are performed for a clockwise (CCW), a counterclockwise (CW), and no (NR) rotor rotation. To further justify our inflow, we compare these inflow profiles resulting from the diurnal cycle simulation to profiles of the Ekman-spiral in the new Eq. 7 and 8. The results show good for a typical SBL value of the eddy viscosity coefficient  $\kappa = 0.05 \text{ m}^2 \text{ s}^{-1}$ . We also point out three different observational studies, from different locations, where such inflow veer has been observed.

These six simulations (SBL\_CR, SBL\_NR, SBL\_CCR, EBL\_CR, EBL\_NR, EBL\_CCR) replace the six existing ones (V\_CCW, V\_NR, V\_CW, NV\_CCW, NV\_NR, NV\_CW) in the previous manuscript version. They have very similar characteristics (wind profiles, potential temperature, turbulence intensity), resulting therefore in similar wake characteristics. Our primary conclusion from the original manuscript persists, that in veered flow, CW rotation and CCW rotation exhibit very different wake characteristics. These results are now presented in Sect. 4: 'A rotating wind-turbine rotor under veering inflow' (Note we changed from CCW (counterclockwise wake) to CR (clockwise rotor), as we think it is more intuitive to give the rotor rotation). Further, the new SBL simulations apply veer limited to the lower rotor half with a larger directional shear in this region than the 'V' simulations in the previous version.)

2. Regarding the modeling part: the authors mentioned that “considering complex entrainment processes, we think the mass has not to be conserved at specific downstream regions, as it is the case over the whole domain”! This statement is not true. The presented model by the authors does not conserve mass and momentum. Therefore, it is incorrect. There are already several existing models in the literature that conserve both mass and momentum conservation, and the authors can refer to those.

There was a misunderstanding with the 'Simplified Wake Model'. Reviewer 1 suggested a comparison to existing wake models, which make us realize that the name 'Simplified Wake Model' was a perhaps misleading choice. Sect. 4 in the previous version was not intended to be a new wake model, comparable to existing well defined ones. It is simply a device to help to explain why a significant difference in the meridional wake component occurs depending on the rotational direction of the rotor under veering inflow conditions.

Therefore, in the revised version of the manuscript we have changed the description and included this presentation and discussion in a very simplified equation in Sect. 3 'Analysis of a rotating system under veering inflow'. We further simplified the rather complex equations in the old version of the manuscript, to one analytic equation (Eq. 17). There is no need to use existing wake models as proposed by the reviewer 1, as we are not proposing a model to be used for other purposes like wake steering, energy production estimates, etc. Rather, we present this discussion to highlight the interaction of two physical processes (wake rotation and inflow veer) only. We subsequently interpret our LES results in light of this model of the interaction of these two physical processes.

## Reviewer 2: Minor revisions

The authors have provided satisfactory response to my comments and I thank them for taking the time to expand on their presentation and clarify a number of items.

We thank the reviewer for the considerable time they have devoted to helping us improve the presentation of our work.

We carefully considered the criticism and the way that we presented this work. Our intent for the paper is to make people aware that a wind turbine's rotational direction has an impact on the wake under veering inflow. Therefore, we perform extensive changes to the simulations, the simple analysis, and the discussion of the results. Our primary conclusion from the original manuscript persists, that in veered flow, CW rotation and CCW rotation exhibit very different wake characteristics. As the basic motivation of the paper is the same, the introduction and conclusion have only minor changes.

A few general comments to the revised version of the manuscript:

- Reviewer 1 was concerned about our turbulence generation method. Therefore we have reverted to using established and published wind and turbulence profiles from LES from a diurnal cycle. We extract non-veered inflow from evening boundary layer (EBL) and veered inflow from stable boundary layer (SBL) portions of published in Boundary-Layer Meteorology, editor Fedorovich (Englberger and Dörnbrack, 2018). We therefore no longer reply on artificial inflow profiles (Eq. 4, and 5 in the previous version). The non-veered EBL and the veered SBL wind-turbine simulations are performed for a clockwise (CCW), a counterclockwise (CW), and no (NR) rotor rotation. To further justify our inflow, we compare these inflow profiles resulting from the diurnal cycle simulation to profiles of the Ekman-spiral in the new Eq. 7 and 8. The results show good for a typical SBL value of the eddy viscosity coefficient  $\kappa = 0.05 \text{ m}^2 \text{ s}^{-1}$ .

These six simulations (SBL\_CR, SBL\_NR, SBL\_CCR, EBL\_CR, EBL\_NR, EBL\_CCR) replace the six existing ones (V\_CCW, V\_NR, V\_CW, NV\_CCW, NV\_NR, NV\_CW) in the previous manuscript version. They have very similar characteristics (wind profiles, potential temperature, turbulence intensity), resulting therefore in similar wake characteristics. Our primary conclusion from the original manuscript persists, that in veered flow, CW rotation and CCW rotation exhibit very different wake characteristics. These results are now presented in Sect. 4: 'A rotating wind-turbine rotor under veering inflow' (Note we changed from CCW (counterclockwise wake) to CR (clockwise rotor), as we think it is more intuitive to give the rotor rotation.) Further, the new SBL simulations apply veer limited to the lower rotor half with a larger directional shear in this region than the 'V' simulations in the previous version.)

Reviewers comments:

I would still like to see quantitative comparison to measurements. The paper reads as, ...trust the simulations, they are believed to represent the relevant physics correctly. Even if data isn't available to compare with every case that was considered, that's fine. That is the power of simulation to extend observation to investigate a broader possible conditions.

Reviewer 2 suggests a quantitative comparison to measurements. However, the LES result from an idealized diurnal cycle simulation. Therefore, no measurements are available for exactly these conditions. However, in the text, we compare the wake structures (skewness under veering inflow etc.) to other studies, to show that the results are reasonable and consistent with previous work, and benefit from the explanation afforded by the simple analysis in the new Sect. 3. Further, the new set of simulations are based on previously published results and so should not incur any questions regarding the turbulence generation method.

What is still lacking in this study is to leverage the advantage of the power of LES to provide information about unsteady phenomena. Otherwise, why do you need LES and not simply run RANS to show the relative behavior.

There was a misunderstanding with the 'Simplified Wake Model', which make us realize that the name 'Simplified Wake Model' was a perhaps misleading choice. Sect. 4 in the previous version was not intended to be a new wake model, comparable to existing well defined ones. It is simply a device to help to explain why a significant difference in the meridional wake component occurs depending on the rotational direction of the rotor under veering inflow conditions, as simplification, for a laminar inflow without any turbulence.

Therefore, in the revised version of the manuscript we have changed the description and included this presentation and discussion in a very simplified equation in Sect. 3 'Analysis of a rotating system under veering inflow'. We further simplified the rather complex equations in the old version of the manuscript, to one analytic equation (Eq. 17). This should highlight the laminar inflow without any turbulence and interaction between the three wind components considered.

We present this analysis to highlight the interaction of two physical processes (wake rotation and inflow veer). We subsequently interpret our LES results in light of this model of the interaction of these two physical processes. Comparing the LES results (with turbulent flow) to the simple analysis (for laminar flow), we highlight the important impact of turbulence and the benefit of using LES for this study.

An example: In the LES of the SBL WT simulations, veer is limited to the lower rotor part. In the analysis (laminar inflow), there is not impact in the upper rotor part in this case, however, we see an impact in the LES SBL WT simulations also in the upper rotor part, which is an effect of the turbulence which is considered in LES.

The addition of the comparison of velocity deficit and total turbulence intensity is helpful. It would be helpful to also include the comparison of velocity

profiles or deficit profiles and turbulence intensity or added turbulence intensity at a couple of wake positions in the vertical and horizontal planes to get a better feel for how the different cases compare. I think this will also help readers interpret the profiles of difference, which are a bit noisy and hard to read.

Reviewer 2 suggested that we include a qualitative investigation of  $u$  and turbulence intensity  $TI$ . This new discussion appears in Sect. 4 as well as in Fig. 11 and 12.

Overall, this is an interesting comparison of cases and clearly a lot of work went into the simulations.  
Thank you!



# Does the rotational direction of a wind turbine impact the wake in a stably stratified atmospheric boundary layer?

Antonia Englberger<sup>1</sup>, Andreas Dörnbrack<sup>1</sup>, and Julie K. Lundquist<sup>2,3</sup>

<sup>1</sup>German Aerospace Center, Institute of Atmospheric Physics, Oberpfaffenhofen, Germany

<sup>2</sup>Department of Atmospheric and Oceanic Sciences, University of Colorado Boulder, Boulder, USA

<sup>3</sup>National Renewable Energy Laboratory, Golden, Colorado, USA

**Correspondence:** Antonia Englberger (antonia.englberger@dlr.de)

**Abstract.** Stably stratified atmospheric boundary layers are often characterized by a veering wind profile, in which the wind direction changes clockwise with height in the Northern Hemisphere. Wind-turbine wakes respond to this veer in the incoming wind by stretching from a circular shape into an ellipsoid. We investigate the relationship between this stretching and the direction of the turbine rotation by means of large-eddy simulations. Clockwise rotating, counterclockwise rotating, and non-rotating actuator disc turbines are embedded in wind fields of a precursor simulation with no wind veer ~~or~~ and in wind fields with ~~an Ekman spiral representative of the Northern Hemisphere~~ Northern Hemispheric Ekman spiral, resulting in six combinations of rotor rotation and inflow wind condition. The ~~impact of the Coriolis force via the Ekman spiral depends on~~ wake strength, extension, width and deflection depend on the interaction of the meridional component of Ekman spiral with the rotational direction of the actuator disc, whereas the direction of the disc rotation ~~exerts little impact only marginally modifies~~ the wake if no veer is present. The differences result from the ~~interaction of the actuator rotation with the Ekman spiral and are present in the zonal, the meridional, amplification or weakening/reversion of the spanwise~~ and the vertical wind components of the wake. The interaction of the Ekman spiral with both rotational directions lead to two different flow fields characterizing the wake due to the effect of the superposed disc rotation. They are also present in the streamwise wind component of the wake and in the total turbulence intensity. In the case of a counterclockwise rotating actuator disc, the ~~rotational direction of the wake persists~~ spanwise and vertical wind components increase directly behind the rotor resulting in the same rotational direction in the whole wake ~~. In~~ while its strength decreases downwind. In the case of a clockwise rotating actuator disc, however, the ~~rotational direction is different~~ spanwise and vertical wind components of the near wake are weakened or even reversed in comparison to the inflow. This weakening/reversion results in a downwind increase of the strength of the flow rotation in the wake or even a different rotational direction in the near wake in comparison to the far wake. The physical mechanism responsible for this difference ~~is~~ can be explained by a simple linear superposition of ~~the inflow wind field, characterized by vertical wind shear and wind veer, with a wind turbine model including a Rankine vortex, representing the rotational effects imposed on the flow by the rotating blades~~ a veering inflow with a Rankine vortex.

*Copyright statement.* The copyright of the authors Antonia Englberger and Andreas Dörnbrack for this publication are transferred to Deutsches Zentrum für Luft- und Raumfahrt e. V., the German Aerospace Center. This work was authored [in part] by the National Re-

newable Energy Laboratory, operated by Alliance for Sustainable Energy, LLC, for the U.S. Department of Energy (DOE) under Contract No. DE-AC36-08GO28308. Funding provided by the U.S. Department of Energy Office of Energy Efficiency and Renewable Energy Wind Energy Technologies Office. The views expressed in the article do not necessarily represent the views of the DOE or the U.S. Government. The U.S. Government retains and the publisher, by accepting the article for publication, acknowledges that the U.S. Government retains a nonexclusive, paid-up, irrevocable, worldwide license to publish or reproduce the published form of this work, or allow others to do so, for U.S. Government purposes.

## 1 Introduction

In wind energy science, the engineering system of a wind turbine interacts with the geophysical system of the atmospheric boundary layer (ABL). The canonical ABL over land experiences a diurnal cycle in prevailing wind and turbulence conditions (Stull, 1988). The diurnal cycle is driven by shortwave heating during the day and radiative cooling at night. Shortwave heating of the surface triggers convective turbulence that mixes throughout the boundary layer, resulting in a well-mixed convective boundary layer (CBL) during day with little vertical wind shear (change of wind speed with height) and high levels of turbulence. The blades of a wind turbine in a CBL are therefore often exposed to the same wind speed and wind direction at each possible blade position. At night, radiative cooling of the surface leads to a decay of the convective turbulence, resulting in a stable boundary layer (SBL), with low turbulence levels and highly sheared wind profiles. The interaction between the Coriolis force ~~acting on the velocity components~~ and friction in the boundary layer will cause winds to rotate with height, ~~approaching the geostrophic wind.~~ This veering of the wind through the boundary layer is described by the ~~hemispheric dependent~~ Ekman spiral. In the Northern Hemisphere, winds will rotate in the clockwise direction with height (i.e. westerly near the surface and northerly aloft), while in the ~~southern hemisphere~~ Southern Hemisphere, winds will rotate in the counterclockwise direction with height (i.e. westerly near the surface and southerly aloft). Therefore, the nighttime wind system in the Northern Hemispheric mid-latitudes is typically characterised by a veering wind (a wind that rotates in a clockwise direction with height) and a pronounced vertical wind shear (Walter et al., 2009). Of course, synoptic events such as frontal passages or topographically-driven phenomena such as drainage flows may modify this typical background veer. The blades of a wind turbine in an SBL therefore do not interact with a uniform flow field in all heights as during day, but with an increasing wind speed with height and also a wind direction change with height.

The stability-dependent wind and turbulence conditions of a wind-turbine inflow determine the entrainment of energy and momentum into the wake region and the resulting wake structure, with fast eroding wakes in convective conditions and wakes persisting ~~further~~ further downwind in stably stratified conditions. This stability dependence has been investigated using large-eddy simulation (LES) for the SBL (Aitken et al., 2014; Bhaganagar and Debnath, 2014, 2015; Dörenkämper et al., 2015), the CBL (Mirocha et al., 2014), both of them (Abkar and Porté-Agel, 2014; Vollmer et al., 2017), or the complete diurnal cycle (Abkar et al., 2016; Englberger and Dörnbrack, 2018a). This stability dependence has also been observed in field campaigns (Jungo et al., 2013; Bodini et al., 2017).

~~The upstream wind and turbulence profiles, characterised by the prevailing atmospheric condition, interact with the rotating blades of a wind turbine. Due~~

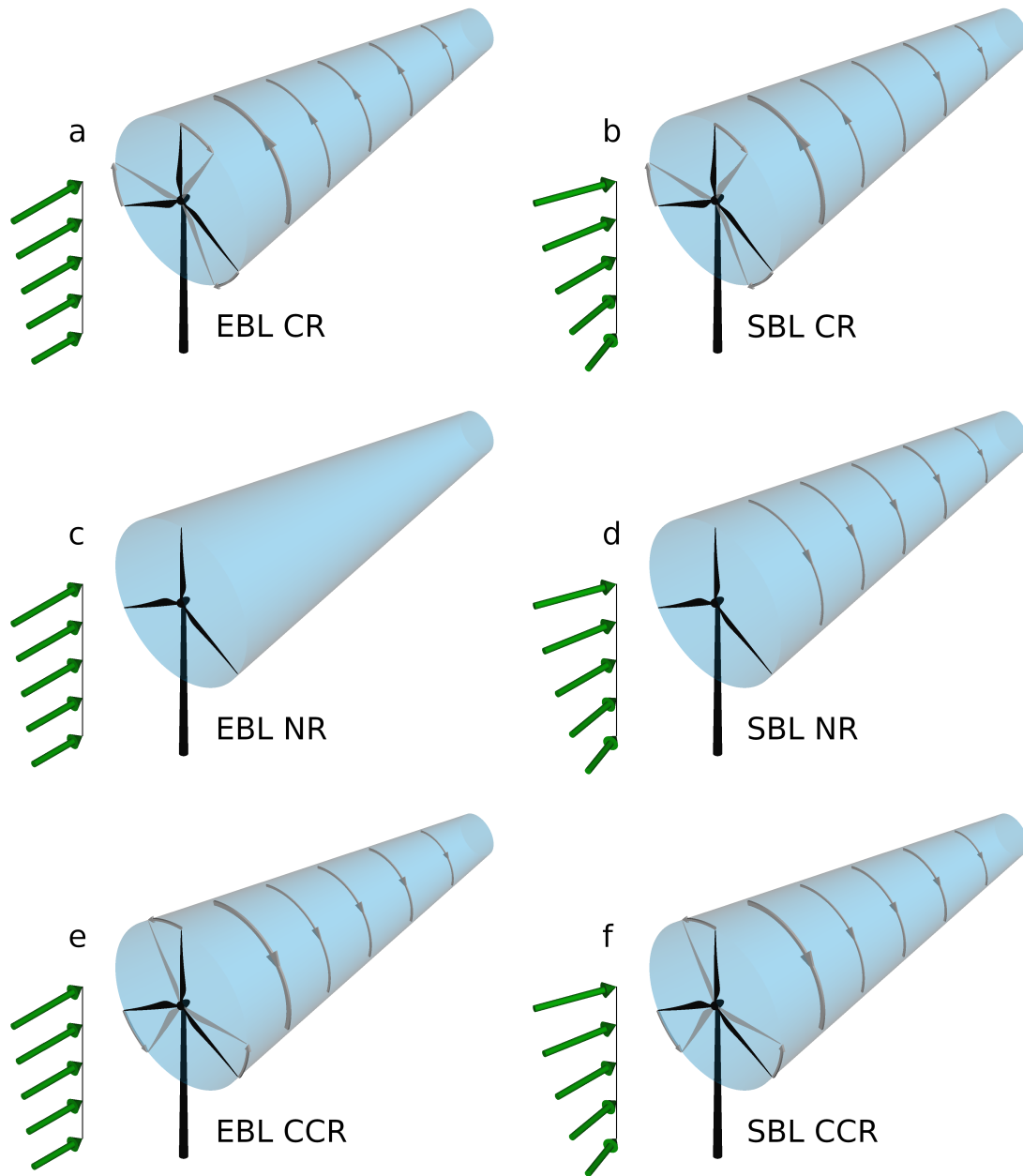


**Figure 1.** Schematic illustration of the rotational direction of the wake for the cases: No wind veer with clockwise blade rotation (EBL CR) in (a), wind veer with clockwise blade rotation (SBL CR) in (b), no wind veer with no blade rotation (EBL NR) in (c), wind veer with no blade rotation (SBL NR) in (d), no wind veer with counterclockwise blade rotation (EBL CCR) in (e), wind veer with counterclockwise blade rotation (SBL CCR) in (f).

All modern multi-MW wind turbines have blades that rotate clockwise when looking downwind at the turbine. Historically, traditional grain-grinding wind mills turned counter-clockwise for ease of manufacturing by right-handed technicians. By market happenstances, described well in Maegaard et al. (2013), the companies building blades in the 1970's evolved from having a mix of clockwise and counterclockwise rotating blades into a market domination of clockwise rotating blades. These clockwise rotating blades exhibit a counterclockwise rotating wake and vice versa (Zhang et al., 2012); due to aerodynamics and design of the wind turbine blades, the ~~rotational direction of most industrial wind turbines is clockwise (while looking downwind). Clockwise rotating blades will exhibit a counterclockwise rotating wake (Zhang et al., 2012)~~ flow moves the blades in one direction and is deflected away from them in the opposite direction. Studies investigating the effect of wind turbine rotors rotating in opposite directions, especially for wind farm optimization, show that the rotational direction has an impact on the wake structure of a wind turbine and therefore on the performance of a downwind turbine (Vermeer et al., 2003; Shen et al., 2007; Sanderse, 2009; Kumar et al., 2013; Hu et al., 2013; Yuan et al., 2014; Mühle et al., 2017). Further, in simulations, representing an array of wind turbines with a second row rotating opposite to the rotation of the first row, an increase in productivity was found in comparison to the co-rotating pair of turbines. This improvement is related to the different direction of the angular component in the wake and therefore the change in the angle of attack on the downwind turbine (Mühle et al., 2017).

~~These studies, which detect a rotational direction impact on the wake; However, these studies~~ were performed for wind conditions without significant vertical wind shear and without wind veer in the rotor altitudes. Vertical wind shear and wind veer ; ~~however, impact the wake characteristics (Abkar and Porté-Agel, 2016; Vollmer et al., 2017; Englberger and Dörnbrack, 2018a) ; and also power production (?). As both effects impact wake characteristics (Abkar and Porté-Agel, 2016; Abkar et al., 2016; Vollmer et al.~~ , power production (Gomez and Lundquist, 2020), as well as turbine loads (Kapoor et al., 2019). Because both shear and veer influence the wake, their interaction in combination with different rotational directions might ~~have a large impact on the impact~~ wake characteristics in stably stratified regimes. This possible impact is investigated in this study in detail, aiming to answer the question:

Does the rotational direction of a wind turbine impact the wake in a stably stratified atmospheric boundary layer?

~~Schematic illustration of the rotational direction of the wake for the cases: Wind veer with clockwise blade rotation (V\_CCW) in (a), no wind veer with clockwise blade rotation (NV\_CCW) in (b), wind veer with no blade rotation (V\_NR) in (c), no wind veer with no blade rotation (NV\_NR) in (d), wind veer with counterclockwise blade rotation (V\_CW) in (e), no wind veer with counterclockwise blade rotation (NV\_CW) in (f).~~

We investigate the relationship between the upstream wind profile ~~and~~ the direction of the turbine rotation ~~by~~ , and the wake by LES. Clockwise-rotating, counterclockwise-rotating and non-rotating actuator discs are embedded in two different atmospheric regimes . ~~The simplest scenario includes only wind shear, specifically an increase of wind speed with height. The more complex scenario also includes veer characteristics of the Northern Hemisphere's Ekman spiral, which are representative of a stably stratified taken from a diurnal cycle simulation from Englberger and Dörnbrack (2018a). The~~ evening boundary layer (EBL) ~~is characterized by a small amount of vertical wind shear with no wind veer. The SBL is characterized by a~~

significant amount of vertical wind shear and wind veer, representing the Northern Hemispheric Ekman spiral. The simulations represent the following six combinations of rotor rotation and wind conditions from shown in Fig. 1. To our knowledge, this study is the first study which investigates investigation of the dependence of wake characteristics on the rotational direction of a rotor and wind veer in a stably stratified ABL.

- 5 The paper is organised as follows. The numerical model EULAG, the metrics, and the wind-turbine simulation setup and the metries are described in Sect. 2. The interaction of rotational direction with wind veer analysis of a rotating system under veering inflow is presented in Sect. 3 and the developed simplified wake model to explain this interaction, and the wake characteristics of a rotating wind-turbine rotor under veering inflow is presented in Sect. 4. The resulting impact of the rotational direction on the flow in the wake is illustrated. A comparison of a rotating wind turbine under veering inflow to analysis predictions is given in Sect. 5. A conclusion follows in Sect. 6.

## 2 Numerical Model Framework

### 2.1 The Numerical Model EULAG

The dry ABL flow through a wind turbine is simulated with the multiscale geophysical flow solver EULAG (Prusa et al., 2008; Englberger and Prusa et al., 2008; Englberger and Dörnbrack, 2017). The acronym EULAG refers to the ability of solving to solve the equations of motion either in an Eulerian (flux form) (Smolarkiewicz and Margolin, 1993) or in a semi-Lagrangian (advective form) (Smolarkiewicz and Pudykiewicz, 1992) mode. The geophysical flow solver EULAG is at least of second-order accurate in time and space (Smolarkiewicz and Margolin, 1998) and well-suited for massively-parallel computations (Prusa et al., 2008). It can be run parallel up to a domain decomposition in three dimensions. A comprehensive description and discussion of the geophysical flow solver EULAG can be found in Smolarkiewicz and Margolin (1998) and Prusa et al. (2008).

- 20 For the numerical simulations conducted for this paper, the Boussinesq equations for a flow with constant density  $\rho_0 = 1.1 \text{ kg m}^{-3}$  are solved for the Cartesian velocity components  $\mathbf{v} = (u, v, w)$  and for the potential temperature perturbations  $\Theta' = \Theta - \Theta_e$  (Smolarkiewicz et al., 2007),

$$\frac{d\mathbf{v}}{dt} = -G\nabla\left(\frac{p'}{\rho_0}\right) + \mathbf{g}\frac{\Theta'}{\Theta_0} + \mathcal{V} + \mathbf{M}\pm_{\mathbf{v}}\frac{\mathbf{F}_{WT}}{\rho_0} - 2\Omega_{\mathcal{C}}(\mathbf{v} - \mathbf{v}_e)\pm_{\mathbf{v}}\beta_{\mathbf{v}}\frac{\mathbf{F}_{WT}}{\rho_0}, \quad (1)$$

$$\frac{d\Theta'}{dt} = \pm_{\mathbf{v}}\nabla\Theta_e + \mathcal{H}, \quad (2)$$

25  $\nabla \cdot (\rho_0 \mathbf{v}) = 0,$  (3)

where  $\Theta_0$  represents the constant reference value. Height dependent states  $\psi_e(z) = (u_e(z), v_e(z), w_e(z), \Theta_e(z))$  enter Eqs. 1 - 3 in the buoyancy term, the Coriolis term, and as boundary conditions. These background states correspond to the ambient and environmental states. Initial conditions are provided for  $u, v, w$ , and the potential temperature perturbation  $\Theta'$  in  $\psi = (u, v, w, \Theta')$ . In Eqs. (1), (2) and (3),  $d/dt$ ,  $\nabla$  and  $\nabla \cdot$  represent the total derivative, the gradient and the divergence, respectively. The quantity

$p'$  represents the pressure perturbation with respect to the background state and  $\mathbf{g}$  the vector of acceleration due to gravity. The factor  $G$  represents geometric terms that result from the general, time-dependent coordinate transformation (Wedi and Smolarkiewicz, 2004; Smolarkiewicz and Prusa, 2005; Prusa et al., 2008; Kühnlein et al., 2012). The subgrid-scale terms  $\mathcal{V}$  and  $\mathcal{H}$  symbolise viscous dissipation of momentum and diffusion of heat and  $\mathbf{M}$  denotes the inertial forces of coordinate-dependent metric accelerations.  ~~$\mathbf{F}_{WT}$  corresponds to the turbine-induced force, implemented with the blade element momentum method as actuator disc without and with rotation ( $\beta_v \in \{-0, -1, 1\}$ ) in the wind turbine simulations.~~ The Coriolis force is represented by the angular velocity vector ~~of the earth~~  $\Omega_C$  of the Earth's rotation. All following simulations are performed with a TKE closure (Schmidt and Schumann, 1989; Margolin et al., 1999).

The axial  $\mathbf{F}_x$  and tangential  $\mathbf{F}_\Theta$  turbine-induced forces ( $\mathbf{F}_{WT} = \mathbf{F}_x + \mathbf{F}_\Theta$ ) in Eq. (1) are parametrized with the blade element momentum (BEM) method as a rotating actuator disc without and with rotation in clockwise and counterclockwise direction ( $\beta_v \in \{0, -1, 1\}$ ), including a nacelle and excluding the tower. ~~This~~ We do not simulate the rotor rotation directly, instead, we exert the rotor forces directly on the velocity fields (Eq. (1)). As a clockwise wake rotation is initiated by a counterclockwise blade rotation, due to conservation of angular momentum (e.g. described in Zhang et al. (2012)), we define a common clockwise rotor rotation as counterclockwise wake rotation with  $\beta_v = 1$  and  $\beta_w = -1$ , a counterclockwise rotor rotation as clockwise wake rotation defined by  $\beta_v = -1$  and  $\beta_w = 1$ , and no rotation is simulated by  $\beta_v = 0$  and  $\beta_w = 0$ , with  $\beta_u = 1$  in each case.

The BEM method accounts for local blade characteristics, as it enables calculation of the steady loads as well as the thrust and the power for different wind speeds, rotational speeds, and pitch angles of the blades. For the airfoil data, the 10 MW reference wind turbine from DTU (Bak et al., 2013) is applied, whereas the radius of the rotor as well as the chord length of the blades are scaled to a rotor with a diameter of 100 m. A more detailed description of the wind-turbine parametrization and the applied smearing of the forces, as well as all values used in the wind-turbine parametrization are given in Englberger and Dörnbrack (2017, parametrization B).

## 2.2 Setup of the Wind-Turbine Simulations

~~Wind-turbine simulations with open horizontal boundaries are performed for a stably stratified lasting 20 min on  $512 \times 64 \times 64$  grid points with a horizontal and vertical resolution of 5 m. The rotor of the wind turbine is located at 300 m in  $x$ -direction and centred in  $y$ -direction with a diameter ( $D$ ) and a hub height  $z_h$ , both 100 m.~~

~~List of all performed simulations in this study. Here,  $V$  refers to veer and  $NV$  to no veer,  $CCW$  to counterclockwise wake rotation,  $CW$  to clockwise wake rotation, and  $NR$  to no rotation of the disc: simulation veer wake rotation  $V\_CCW$  yes counterclockwise  $V\_NR$  yes no  $V\_CW$  yes clockwise  $NV\_CCW$  no counterclockwise  $NV\_NR$  no no  $NV\_CW$  no clockwise~~

~~In the scope of this paper, we performed six wind turbine simulations, listed in Table ?? and schematically plotted in Fig. 1. These simulations differ by two main components, the presence of veer and the rotational direction of the wake.~~

All simulations are initialized with the zonal velocity profile including vertical wind shear ( $\frac{\partial u}{\partial z} \neq 0$ )

$$u_{BL}(z) = u_g \cdot \left( 1 - \exp\left(-\frac{z\sqrt{f/\kappa}}{\sqrt{2}}\right) \right),$$

with a geostrophic wind  $u_g = 10 \text{ m s}^{-1}$ , the Coriolis parameter  $f = 1.0 \times 10^{-4} \text{ s}^{-1}$ , and an eddy viscosity coefficient  $\kappa = 0.06 \text{ m}^2 \text{ s}^{-1}$ , following Shapiro and Fedorovich (2010). In the simulations with wind veer ( $\frac{\partial v}{\partial z} \neq 0$ ), the wind direction change over the

5 100-m rotor disc is  $8^\circ$  with  $v_{BL}(z_h) = 0$ . The meridional velocity profile is therefore

$$v_{BL}(z) = u_{BL}(z) \cdot \tan\left(\left(270^\circ - \left(262^\circ + 8^\circ \frac{z}{100\text{m}}\right)\right) \frac{\pi}{180^\circ}\right)$$

in the lowest 200 m and constant above. A wind veer of  $0.08^\circ \text{ m}^{-1}$  represents a nighttime situation, following Walter et al. (2009) and is in agreement with measurements (Walter et al., 2009; Bodini et al., 2019b; Gomez and Lundquist, 2020) indicating that a veer in excess of  $0.2^\circ \text{ m}^{-1}$  does occur. In simulations without wind veer, the meridional velocity profile is

10  $v_{BL}(z) = 0.$

The vertical velocity is

$$w_{BL}(z) = 0$$

in all simulations.

Three different wake conditions are considered: Clockwise wake rotation (*CW*), no wake rotation (*NR*), and counterclockwise  
 15 wake rotation (*CCW*), defined from a view looking downwind at the wind turbine. In this simulations, only the prefactors  $\beta_v$  and  $\beta_w$  in Eq. (1) differ. A clockwise wake rotation is defined by  $\beta_v = -1$  and  $\beta_w = 1$ , a counterclockwise wake rotation by  $\beta_v = 1$  and  $\beta_w = -1$ , and no rotation by  $\beta_v = 0$  and  $\beta_w = 0$ , with  $\beta_u = 1$  in each simulation. A clockwise wake rotation is initiated by a counterclockwise blade rotation, due to conservation of angular momentum (e.g. described in Zhang et al. (2012)). We do not simulate the rotor rotation, instead, we exerted the rotor forces directly on the velocity fields (Eq. (1)). Therefore, in the  
 20 following we will refer to different wake rotations, which, however, can be linked directly towards the opposite blade rotation. Most wind turbines rotate in the clockwise direction, resulting in a counterclockwise wake rotation, so the *CCW* simulations represent the typical situation.

The parametrization of Englberger and Dörnbrack (2018b) is applied to represent a turbulent stably stratified regime in a wind-turbine simulation with open horizontal boundary conditions. All parameters required to apply the parametrization are  
 25 described in detail in Englberger and Dörnbrack (2018b). The parametrization includes the same turbulent intensity in all performed idealized simulations, so therefore the only differences are the veer or no veer cases or the rotational direction of the disc. Further, the applied parametrization makes the numerically efficient and computationally fast (about 1 min wall time to simulate 1 min model time on 64 Intel Xeon E5-2697 v3 threads at 2.6 GHz). Both aspects make the parametrization well suited for this case study.

## 2.2 Metrics

List of grid points (gp) considered for the sectors applied in the evaluation. Right and left correspond to the rotor section from a view upwind of the wind turbine on the rotor with radius  $R$ : sector top tip right bottom tip left  $60^\circ$  gp  $\leq 30^\circ$  or gp  $\geq 330^\circ$   $60^\circ \leq$  gp  $\leq 120^\circ$   $150^\circ \leq$  gp  $\leq 210^\circ$   $240^\circ \leq$  gp  $\leq 300^\circ$   $90^\circ$  gp  $\leq 45^\circ$  or gp  $\geq 315^\circ$   $45^\circ <$  gp  $< 135^\circ$   $125^\circ \leq$  gp  $\leq 225^\circ$   $225^\circ <$  gp  $< 315^\circ$

5

Schematic illustration of the top-tip sector (tt), the bottom-tip sector (bt), as well as the right and left sectors, defined from a view looking downwind toward the wind turbine on the disc. All sectors are  $60^\circ$  and  $25 \text{ m} \leq r \leq 50 \text{ m}$  sectors.

For the investigation of the dependence of wake characteristics on the wake rotation and wind veer, the following characteristics are used calculated from the simulation results: the spatial distribution of the time-averaged discrete streamwise velocity  $\overline{u_{i,j,k}}$ , the time-averaged discrete spanwise velocity  $\overline{v_{i,j,k}}$ , the time-averaged discrete vertical velocity  $\overline{w_{i,j,k}}$ , and the streamwise velocity deficit

10

$$VD_{i,j,k} \equiv \frac{\overline{u_{1,j,k}} - \overline{u_{i,j,k}}}{\overline{u_{1,j,k}}}, \quad (4)$$

the streamwise ( $x$ ), spanwise ( $y$ ) and vertical ( $z$ ) turbulence intensity, e.g. in  $x$  direction

$$TI_{x_{i,j,k}} = \frac{\sigma_{u_{i,j,k}}}{\overline{u_{i,j,k}}}, \quad (5)$$

15

with  $\sigma_{u_{i,j,k}} = \sqrt{u_{i,j,k}'^2}$  and  $u_{i,j,k}' = u_{i,j,k} - \overline{u_{i,j,k}}$ . Similar formulas apply for  $TI_y$  and  $TI_z$  in the  $y$ , and  $z$  directions respectively. The total turbulence intensity is

$$TI_{i,j,k} = \sqrt{\frac{1}{3}(TI_{x_{i,j,k}}^2 + TI_{y_{i,j,k}}^2 + TI_{z_{i,j,k}}^2)}. \quad (6)$$

The indices of the grid points are denoted by  $i = 1 \dots n$ ,  $j = 1 \dots m$  and  $k = 1 \dots l$  in the  $x$ ,  $y$  and  $z$  directions, respectively. These characteristics are averaged over the last 1050 min of the corresponding 20 min 1 h wind-turbine simulation. The temporal average is calculated online in the numerical model and updated at every timestep according to the method of Fröhlich (2006, Eq. 9.1).

20

In the following, the quantities  $\overline{u_{i,j,k}}$ ,  $\overline{v_{i,j,k}}$ , and  $\overline{w_{i,j,k}}$  are evaluated and discussed downwind of the wind turbine up to 20 D. Further, the rotor area is divided into four sections of 6090°, as shown in Fig. 2, including all grid points with a distance  $r$  from the rotor center  $R/2 \leq r \leq R$ , referred to hereafter as top tip, right, bottom tip, and left (see Table ?? and Fig. 2). These sectors include radial points with 25 m sector, bottom sector, northern sector and southern sector, looking from upwind ( $i \leq r$ ) downwind toward the actuator. In this work, we refer to the left sector as northern sector and to the right sector as southern sector, defined from a view looking downwind from west to east towards the wind turbine on the disc. This naming results from a zonal wind from west to east representing the streamwise flow and a meridional wind from south to north representing the spanwise flow through the wind turbine in the analyzed regimes of this work. However, the results of this work are valid independent of the wind direction of the streamwise and spanwise flow through the wind turbine. In any considered case, a left sector replaces the northern sector and a right sector replaces the southern sector.

30



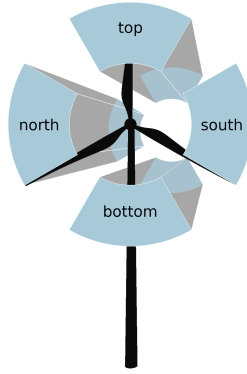


**Figure 2.** Schematic illustration of the top sector, the bottom sector, as well as the southern and northern sectors, defined from a view looking downwind from west to east towards the wind turbine on the disc. All sectors are  $90^\circ$  with  $25 \text{ m} \leq r \leq 50 \text{ m}$ .

### 2.3 Setup of the Wind-Turbine Simulations

In this work, a wind turbine is placed in two different regimes characteristic of different parts of the diurnal cycle: the EBL and the SBL. Both regimes develop from a diurnal cycle precursor simulation over a homogeneous surface with periodic horizontal boundary conditions (Englberger and Dörnbrack, 2018a). The simulation includes  $512 \leq x \leq 50512$  grid points in the horizontal direction with a resolution of 5 m. The vertical resolution is also 5 m in the lowest 200 m, which represent the outer rotor region. We also evaluate the characteristics with  $90^\circ$  sectors (Table ??) or for  $0 \text{ m} < r \leq 50 \text{ m}$  representing the whole rotor (excluding nacelle region) stretching up to the top of the domain at 2 km. The precursor simulation is initialized with a geostrophic wind of  $10 \text{ m s}^{-1}$  as zonal (west-east) wind and no meridional (south-north) and vertical wind. The initial potential temperature is set to a constant value of 300 K up to 1 km, increasing above with a lapse rate of  $10 \text{ K km}^{-1}$ . A sensible heat flux forces the diurnal cycle with a maximum of  $140 \text{ W m}^{-2}$  during day and a minimum of  $-10 \text{ W m}^{-2}$  during night. The diurnal cycle simulation is initialized at 0000 UTC. For the EBL regime, a 1 h time period from 1800 UTC to 1900 UTC is extracted. During this time period the surface fluxes changes sign. For the SBL regime, the selected 1 h time period starts at 0000 UTC (24 h after initialization). The resulting values of all four combinations are comparable between the horizontally averaged zonal ( $u$ ) and meridional ( $v$ ) velocity profiles, the vertical potential temperature ( $\Theta$ ) profile, the total turbulence intensity ( $TI$ ) (Eq. 6) and the turbulence intensities in x, y, and z direction ( $TI_x, TI_y, TI_z$ ) (Eq. 5) of the beginning of the corresponding atmospheric regime are presented in Fig. 3.

Three factors distinguish the EBL and the SBL from each other: First, the meridional wind  $v$  is zero with  $\frac{\partial v}{\partial z} = 0$  and  $90^\circ$  segments, and between the  $0 \text{ m}$  in the EBL, whereas the  $v$ -component in the SBL is larger than zero with  $\frac{\partial v}{\partial z} \neq 0$  for  $z < r \leq 50 \text{ m}$  and  $25 \text{ m} \leq 100 \text{ m}$  (Fig. 3(a)). This veering wind at night is the main difference to the non-veered wind in the EBL. The resulting wind direction change with height in the SBL is an effect of the Coriolis force acting on the velocity components and friction due to the surface in combination with low levels of turbulence due to radiative cooling of the surface

at night. The veering wind profiles correspond to the Ekman spiral with

$$\gamma = \sqrt{\frac{f}{2\kappa}}$$

for a Coriolis parameter  $f = 1.0 \times 10^{-4} \text{ s}^{-1}$  and an eddy viscosity coefficient  $\kappa = 0.05 \text{ m}^2 \text{ s}^{-1}$ , which is an appropriate value for an SBL regime (Yamada and Mellor, 1975). This

5 results in the zonal and meridional wind profiles representing the Ekman spiral

$$2u_{Ekman}(z) = u_g \cdot (1 - \exp(-z\gamma) \cos(z\gamma)), \quad (7)$$

$$v_{Ekman}(z) = u_g \cdot (\exp(-z\gamma) \sin(z\gamma)), \quad (8)$$

following Stull (1988), with a geostrophic wind  $u_g = 50 \text{ m s}^{-1}$ , these values are applied for the derivation of the sector characteristics in the following.

### 10 3 Interaction of Rotational Direction with Wind Veer

Coloured contours of the streamwise velocity  $\overline{u_{i,j,k_h}}$  in  $\text{m s}^{-1}$  at hub height  $k_h$ , averaged over the last 10 min, for V\_CCW in (a), NV\_CCW in (b), V\_NR in (c), NV\_NR in (d), V\_CW in (e), and NV\_CW in (f). The black contours represent the velocity deficit  $VD_{i,j,k_h}$  at the same vertical location.

15 Coloured contours of the streamwise velocity  $\overline{u_{i,j,k_*}}$  in  $\text{m s}^{-1}$  at  $z_h = 125 \text{ m}$  with index  $k_*$ , averaged over the last 10 min, for the same cases as in Fig. ???. The black contours represent the velocity deficit  $VD_{i,j,k_*}$  at the same vertical location.

Coloured contours of the streamwise velocity  $\overline{u_{i,j,k_*}}$  in  $\text{m s}^{-1}$  at  $z = 75 \text{ m}$  with index  $k_*$ , averaged over the last 10 min, for the same cases as in Fig. ???. The black contours represent the velocity deficit  $VD_{i,j,k_*}$  at the same vertical location.

Coloured contours of the streamwise velocity  $\overline{u_{i,j,k_h}}$  in  $\text{m s}^{-1}$  at a downward position of 5 D behind the rotor, averaged over the last 10 min, for V\_NR in (a) and NV\_NR in (b). The black contour represents the actuator.  $10 \text{ m s}^{-1}$  in Fig. 3(a).

20 The relationship between wind veer and the direction of Second, the turbine rotation is investigated with  $x$ -potential temperature profiles differ between the EBL and the SBL (Fig. 3(b)). The sensible heat flux of  $-10 \text{ W m}^{-2}$  during night leads to a maximum cooling close to the surface in the SBL regime, whereas  $\frac{\partial \theta}{\partial z}$   $y$ -cross sections of the streamwise velocity at  $100 \text{ m}$  hub height 0 in the EBL regime when the surface fluxes changes sign and are therefore very small.

Finally, the EBL and the SBL also differ in the amount of turbulence in the atmosphere. Shortwave heating of the surface during day triggers convective turbulence. The EBL still experiences well mixed turbulence, resulting in higher levels of turbulence intensity in comparison to the SBL, with a minor variation in height of  $TI_z$ ,  $TI_x$ , and  $TI_y$  (Fig. ??), in the top half of the rotor disc at  $125 \text{ m}$  (3(c)). At night, radiative cooling of the surface results in negative buoyancy which damps turbulence. Therefore, the total turbulence intensity as well as all three individual components of  $TI$  are smaller in the SBL regime in comparison to the EBL regime (Fig. ??), and in the bottom half of the rotor disc at  $75 \text{ m}$  (3(c)). A more detailed description of the diurnal cycle parameters from Fig. ??) is presented in Englberger and Dörnbrack (2018a).

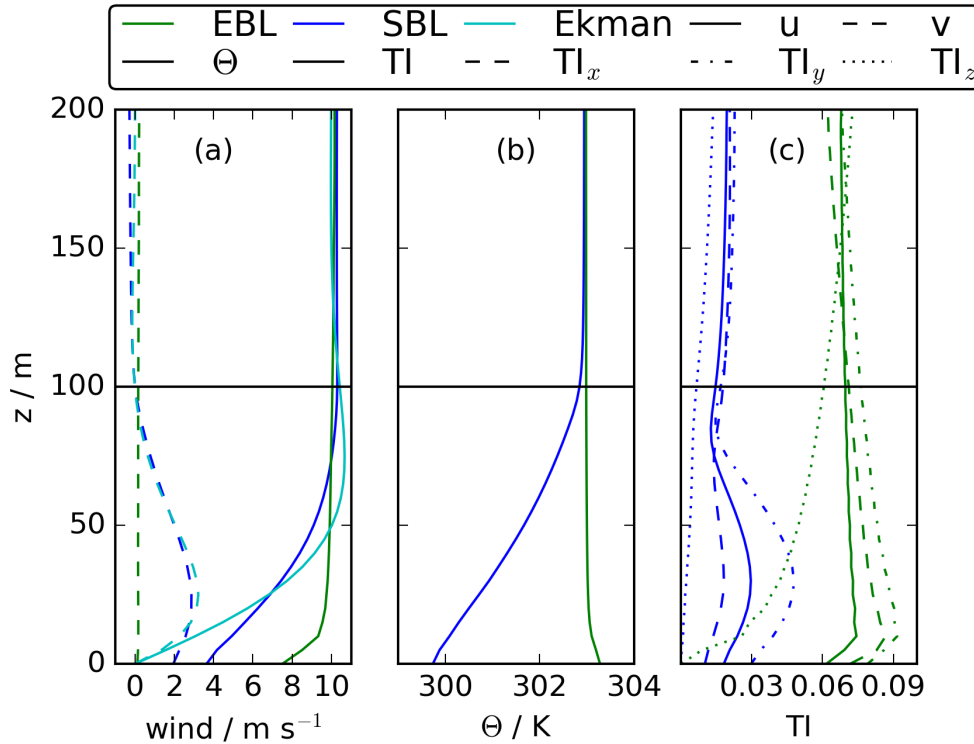


**Figure 3.** Vertical profiles of the horizontal wind components  $u$  and  $v$  in (a), the potential temperature  $\Theta$  in (b), and the total  $TI$ , streamwise  $TI_x$ , spanwise  $TI_y$ , and vertical turbulence intensity  $TI_z$  in (c). The profiles represent the horizontal averages of the EBL and the SBL-regimes in the precursor diurnal cycle simulation.

In a first step, we compare the two non-rotating simulations with and without veer,  $V\_NR$  and  $NV\_NR$ , in Figs. ??(e) vs. (d), ??(e) vs. (d), and ??(e) vs. (d). This comparison reveals the effect of pure wind veer without disc rotation on the wake structure. Firstly, the elongation of the wake at hub height differs. The delayed wake recovery in  $NV\_NR$  is only due to missing wind veer, as the inflow turbulent intensity is the same in the veered and the non-veered cases. In the veered simulation (Fig. 5 ??(e)), the combination of vertical wind shear and wind veer causes the skewed spatial structure in Fig. 7(a). This enhanced production of turbulent kinetic energy due to shear results in a larger entrainment of ambient air and therefore in a more rapid flow recovery in the wake. The skewed structure under veered inflow conditions is similar to those of the simulations of Abkar and Porté-Agel (2016), Vollmer et al. (2017), and Englberger and Dörnbrack (2018a).

Secondly, the wake deflection angle in the top and the bottom half of the rotor disc differs between the veer and no-veer case. The direction of the wake center line derives from the incoming wind veer, resulting in the opposite behaviour between the upper and the lower half of the rotor. Likewise, The EBL regime and the SBL regime represent the two atmospheric regimes in the corresponding wind-turbine simulations. The wind-turbine simulations are performed with periodic boundary conditions in  $y$ -direction and open boundary conditions in  $x$ -direction. To integrate a turbulent regime in the wind-turbine simulations

with open streamwise boundary conditions, a synchronized coupling between the EBL/SBL regime and the upper-half of the wake deflects to the south (Figs. ??(e)) while the lower half of the wake deflects to the north (Figs. ??(e)) (Fig. 3(a)). In contrast, the wake for NV\_VR (Figs. ??(d) and (b)) at 1800 UTC/0000 UTC are applied as initialization of the corresponding wind-turbine simulation. Their horizontal averages are the background fields  $\psi_e(z) = (u_e(z), v_e(z), w_e(z), \Theta_e(z))$ . At each timestep, two dimensional  $y$ - $z$  slices represent the upstream values of  $\psi$  at the left-most edge of the domain. This technique is similar to Kataoka and Mizuno (2002), Naughton et al. (2011), Witha et al. (2014), and Dörenkämper et al. (2015) and has successfully been applied in Englberger and Dörnbrack, where also a more detailed description is provided.

Further, the wind-turbine simulations are performed on  $512 \times 512 \times 64$  grid points with a horizontal resolution of 5 m and a vertical resolution of 5 m in the lowest 200 m and 10 m above. The rotor with  $R = 50$  m and  $z_h = 100$  m is located at 300 m in  $x$ -direction and centered in  $y$ -direction. The wind-turbine simulations are performed with a rotation frequency of  $\Omega = 0.117 \text{ s}^{-1}$  for 10 min and after restart continued for 50 min.

Three different working conditions of the rotor are considered: A common clockwise rotating rotor (CR), a counterclockwise rotating rotor (CCR), and no rotation of the rotor (NR), defined from a view looking downwind on the turbine (Fig. 2). In the simulations of the considered working conditions in the same atmospheric regime, only the prefactors  $\beta_v \in \{0, -1, 1\}$  (Eq. 1) differ, as explained above.

### 3 Analysis of a rotating system under veering inflow

The aim of this work is to investigate if the rotational direction of a wind turbine impacts the wake. As a first step, we summarize the basic physics underlying the interaction process of a rotating system with a veering inflow.

A rotating system can be described by a Rankine vortex, which combines a solid body rotation describing the rotating system with radius  $R$ , with a potential vortex for  $r > R$ . The rotational velocity of the system is expressed by  $\omega$ . The radial dependence of the tangential velocity is given by:

$$v_{\text{tangential}}(r) = \begin{cases} \omega r & r \leq R \\ \omega \frac{R^2}{r} & r > R \end{cases}$$

Consider a rotating system with a rotation area perpendicular to the  $x$ -direction (west-east). The flow components (subscript  $f$ ) in meridional  $v_f$  and vertical  $w_f$  direction interact with the rotating system and are modified by the velocity component of the vortex (subscript  $v$ )  $v_v$  and  $w_v$ . The interaction of the flow and the vortex components modify the flow in the wake  $v$  and  $w$  by:

$$2v_v = \pm \omega r \sin(\Theta), \quad (9)$$

$$w_v = \mp \omega r \cos(\Theta), \quad (10)$$

where the signs  $\pm$  in Eq. 9 and  $\mp$  in Eq. 10 define the rotational direction of the flow in the wake.

For an inflow, interacting with the rotating system, the Ekman spiral (Eqs. 7 and 8) is applied as

$$u_f(z) = u_{Ekman}(z), \quad (11)$$

Regarding the meridional wind component, two cases are possible:

$$5 \quad \text{Case A:} \quad \frac{\partial v}{\partial z} = 0 \rightarrow v_f(z) = 0 \quad (12)$$

$$\text{Case B:} \quad \frac{\partial v}{\partial z} \neq 0 \rightarrow v_f(z) = v_{Ekman}(z). \quad (13)$$

The vertical velocity is

$$w_f(z) = 0. \quad (14)$$

10 Assuming a simple linear superposition of the atmospheric flow with the Rankine vortex, the interaction process modifies the flow in the wake according to:

$$2v(z) = v_f(z) + v_v(z),$$

$$w(z) = w_f(z) + w_v(z).$$

15 In the following, we focus on the meridional flow component  $v$  (Eqs. 12 and 13). We do not need to consider the vertical flow component  $w$  as there is no difference between case A and B in Eq. 14, resulting in Eq. 10 for both cases. Only the  $v$ -component differs between case A (Eq. 12) and B (Eq. 13).

$$2 \text{Case A: } v(z) = v_v(z) = \pm \omega r \sin(\Theta) \quad (15)$$

$$\text{Case B: } v(z) = v_f(z) + v_v(z) = u_g \cdot \exp(-z\gamma) \sin(z\gamma) \pm \omega r \sin(\Theta) \quad (16)$$

20 The rotational direction of the system (defined by  $+$  or  $-$  in Eq. 9 and  $-$  or  $+$  in Eq. 10) has a significant impact on  $v(z)$ , especially in case B (Eq. 16). Depending on the sign of  $v_v(z)$ , the meridional velocity of the inflow  $v_f(z)$  can either be intensified or decelerated or even reversed in the wake. This modification of  $v(z)$  peaks directly behind the rotating system, as the strength of the vortex induced by the rotor  $v_v(z)$  decreases downwind as the flow conditions in the wake approach the inflow value  $v_f(z)$ . The position of complete wake recovery  $x_c$  is defined as the downwind position where  $v_v(z)$  approaches zero and  $v(z) = \theta \cdot v_f(z)$ . To simplify the complex wake entrainment process, we define a linear decrease of  $v_v(z)$  between the  
25 rotating system and downwind distance  $x_c$  by Eq. 17, for a given downstream distance from the rotating system  $x_{down}$ :

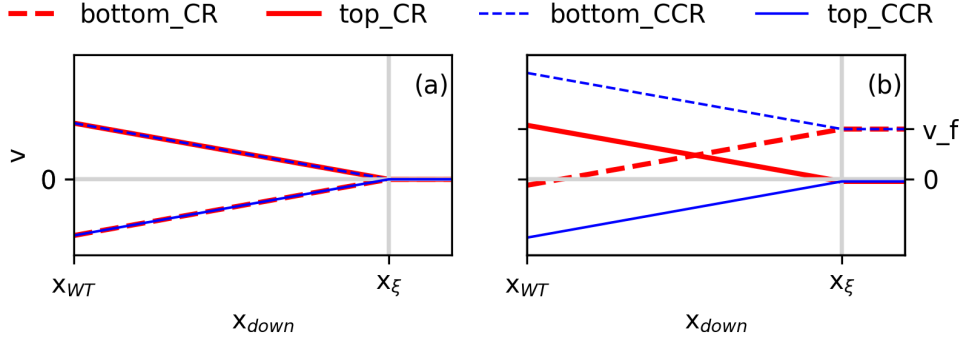


**Figure 4.** Downstream dependence of  $v(z, x_{down})$  at  $z = z_h - R$  as 'bottom' and  $z = z_h + R$  as 'top' considering a center of the rotating system at  $z_h$  with a radius  $R$ .  $CR$  and  $CCR$  correspond to the clockwise and counterclockwise rotational direction of the rotor.

To investigate the effect of wind veer on commonly clockwise rotating wind turbines, we compare  $V_{CCW}$  to  $NV_{CCW}$ , in Figs. ??(a) vs. (b), ??

$$v(z, x_{down}) = \begin{cases} \text{case A:} & \begin{cases} \pm \omega r \sin(\Theta) \left(1 - \frac{x_{down}}{x_\zeta}\right) & x_{down} < x_\zeta \\ 0 & x_{down} \geq x_\zeta \end{cases} \\ \text{case B:} & \begin{cases} u_g \cdot \exp(-z\gamma) \sin(z\gamma) \pm \omega r \sin(\Theta) \left(1 - \frac{x_{down}}{x_\zeta}\right) & x_{down} < x_\zeta \\ u_g \cdot \exp(-z\gamma) \sin(z\gamma) & x_{down} \geq x_\zeta \end{cases} \end{cases} \quad (17)$$

We can consider the wake behaviour in the lower rotor half separately from the wake behaviour in the upper rotor half of a rotating system, with a rotor center  $z_h = 100$  m and a rotor radius  $R = 50$  m (Figure 4). In Figure 4(a) vs., we see case A while in Fig. 4(b), and ??(a) vs. (b). The veer causes a more rapid wake recovery in the top half of the rotor we see case B from Eq. 17. The profiles labeled as bottom correspond to  $v(z_h - R, x_{down})$  and top to  $v(z_h + R, x_{down})$ . The inflow in case B is characterised by the Ekman spiral (Eqs. 7, 8), resulting in a directional shear  $ds$  over the lower rotor part of  $0.23^\circ \text{ m}^{-1}$  (Fig. ??3(a) vs. Fig. ??(b)) as well as in the bottom half. The revolutions per minute of the wake vortex are set to  $1/5 ds = \omega = 0.046 \text{ s}^{-1}$  for both cases.

For both case A and case B, the wake behaviour at top and bottom of the rotor depends on the sign applied in Eq. 17. If '+' is applied in the lower rotor part of case A (Fig. ??4(a) vs. Fig. ??(b)), No significant effect of veer appears in wake recovery at hub height,  $v_v(z_h - R, x_{down})$  flows from north to south ( $v_v(z_h - R, x_{down}) = +\omega r \sin(270^\circ) = -\omega r < 0$ ), corresponding to a counterclockwise wake rotation arising from a clockwise rotor rotation (CR). The interaction of the inflow with the vortex leads to  $v(z_h - R, x_{down}) < 0 \text{ m s}^{-1}$  in the near wake and a linear increase up to  $v(z_h - R, x_\xi) = v_f(z_h - R) = 0 \text{ m s}^{-1}$  at  $x_{down} = x_\xi$ . If '-' is applied in the lower rotor part of case A (Fig. ??4(a) vs. Fig. ??(b)),

Further, inflow wind veer causes wake deflection in both the top half (Fig. ??(a) vs.),  $v_v(z_h - R, x_{down})$  flows from south to north ( $v_v(z_h - R, x_{down}) = -\omega r \sin(270^\circ) = \omega r > 0$ ). This situation corresponds to a clockwise wake rotation and a

counterclockwise rotor rotation (CCR). In case of CCR, the interaction of the inflow with the vortex leads to  $v(z_h - R, x_{down}) > 0 \text{ m s}^{-1}$  in the near wake and a linear decrease up to  $v(z_h - R, x_\epsilon) = v_f(z_h - R) = 0 \text{ m s}^{-1}$  at  $x_{down} = x_\epsilon$ . In the upper rotor half of case A, the situation for  $v(z_h + R, x_{down})$  is the same as in the lower rotor half, only with the opposite sign of  $v(z_h - R, x_{down})$  applied in Eq. 17 (Fig. ??(b) and the bottom half 4(a)).

- 5 Veer can be constrained to the lower half of the rotor, as seen in case B (Fig. ??(a) vs. Fig. ??(b)) of the rotor disc 4(b)). Then it is characterized by a zonal wind from west to east ( $u_f(z_h - R) > 0$ ) with a meridional component from south to north ( $v_f(z_h - R) > 0$ ) in the lower rotor half and a meridional wind component of zero ( $v_f(z_h + R) = 0 \text{ m s}^{-1}$ ) in the upper rotor half. In the non-veered simulation NV\_CCW, the wake is slightly deflected towards the north in the top-tip sector (Fig. ??(b)) and towards the south in the bottom-tip sector (following, the situation for the lower rotor half is discussed, as the upper
- 10 rotor half of case B corresponds to the behaviour of the upper rotor half of case A. In case of CCR,  $v_v(z_h - R, x_{down}) > 0$ , and therefore also flows from south to north. The vortex  $v_v(z_h - R, x_{WT} + \epsilon)$  intensifies the inflow  $v_f(z_h - R)$ , resulting in  $v(z_h - R, x_{WT} + \epsilon) = v_f(z_h - R) + v_v(z_h - R, x_{down})$  directly behind the rotor, with  $\epsilon \ll R$ . Approaching downwind, the vortex impact  $v_v(z_h - R, x_{down})$  and therefore also the flow in the wake  $v(z_h - R, x_{down})$  decreases approaching  $v_f(z_h - R)$  at  $x_\epsilon$ .
- 15 In case of CR,  $v_v(z_h - R, x_{down}) < 0 \text{ m s}^{-1}$ , and therefore flows from north to south, weakening the inflow  $v_f(z_h - R)$ . Therefore, in comparison to  $v_f(z_h - R)$ ,  $v(z_h - R, x_{down})$  decreases in the case of  $|v_v(z_h - R, x_{down})| < |v_f(z_h - R)|$  or even reverses the sign if  $|v_v(z_h - R, x_{down})| > |v_f(z_h - R)|$ , as it is the case in Fig. ??4(b)). Approaching downwind, the vortex impact  $v_v(z_h - R, x_{down})$  decreases and therefore the flow in the wake  $v(z_h - R, x_{down})$  increases up to  $x_\epsilon$  where  $v(z_h - R, x_\epsilon) = v_f(z_h - R)$  and  $x_v(z_h - R, x_\epsilon) = 0 \text{ m s}^{-1}$ . Compared to-
- 20 Summarizing, the analysis predicts a significant difference in the wake flow of a rotating system for a clockwise rotating rotor in comparison to a counterclockwise rotating rotor, but only in the case of a veering inflow (case B).

#### 4 A rotating wind-turbine rotor under veering inflow

- Of course, this rotating rotor interacting with a veering inflow represents a wind turbine operating in nighttime stably stratified atmospheric conditions. To investigate the impact in a turbulent atmosphere for both cases presented in the analysis, here the
- 25 non-veering inflow of an EBL situation and the veering inflow of an SBL situation are considered. For numerical details of the EBL and SBL precursor simulations and the corresponding wind-turbine simulations, we refer to Sect. 2.

##### 4.1 Impact on spanwise and vertical velocity

- As suggested by the analysis of Sect. 3, the rotational direction impact is limited to the change of the sign in Eq. 17 when the inflow lacks veer, as in the EBL. This behaviour is investigated by assessing the wake characteristics of an EBL wind-turbine
- 30 simulation, which are presented in the non-deflected wake in NV\_NR (Figs. ??(d), ?? y-z-plane  $x = 3 \text{ D}$  or  $5 \text{ D}$  in Fig. 5. The top row (Fig. 5(a) - (d)), this effect is caused by the rotation represents the vectors  $(v, w)$ . As expected, the rotational direction of the flow in the wake inside the rotor region is dictated by the rotational direction of the rotor, which transports higher

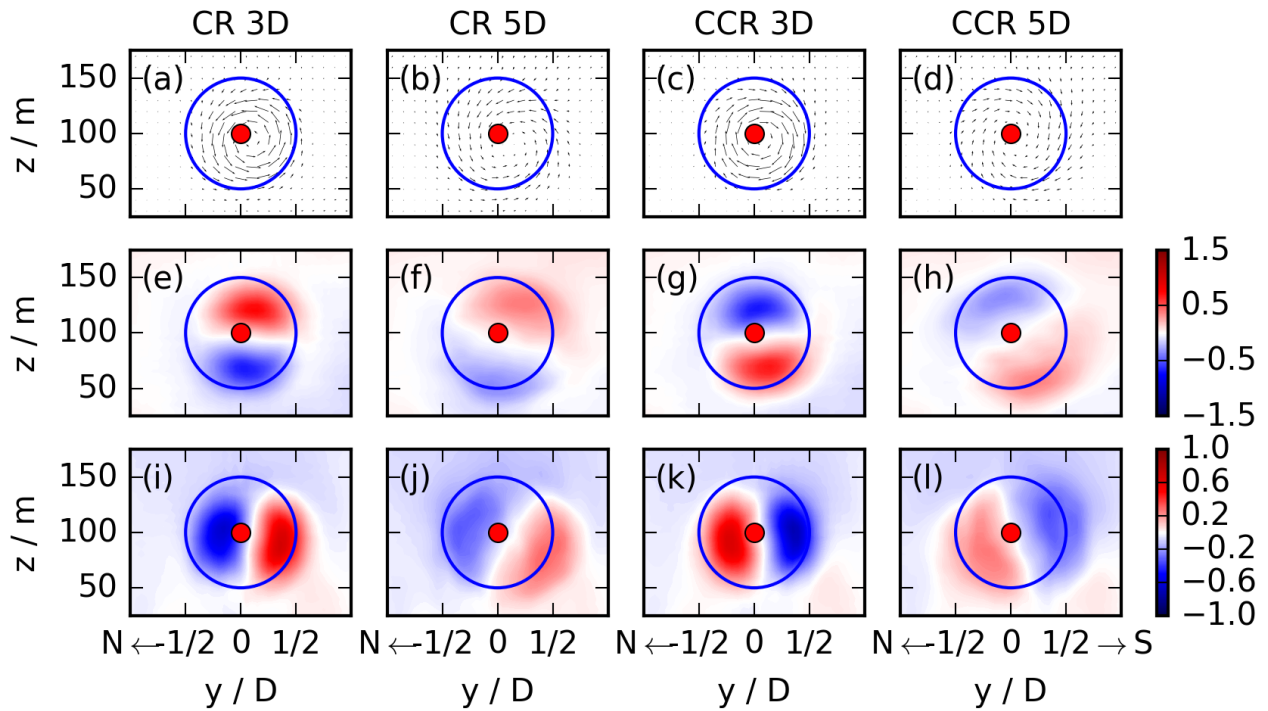


**Figure 5.**  $y$ - $z$ -cross sections of the EBL wind-turbine simulations for CR and CCR at  $x=3D$  and  $5D$ . The first row ((a)-(d)) presents the  $(v, w)$  vectors in the  $y$ - $z$ -plane, the second row ((e)-(h)) the meridional wake velocity  $v$ , and the third row ((i)-(l)) the vertical wake velocity  $w$ . The blue contour represents the circumference of the actuator. The streamwise flow is from the west and these cross sections correspond to a view towards the east downwind through the turbine with north on the left and south on the right.

momentum air counterclockwise, resulting in a northward wake deflection at 125 m. Consequently, the opposite situation prevails at 75 m. The wake in the veered simulation  $V\_CCW$  is deflected towards the south (north) itself and is opposite to the rotor rotation. Approaching downwind from  $x=3D$  to  $5D$ , the rotational direction imprint of the wind-turbine wake decreases.

- 5 The interactions between the wake rotation and the inflow are embodied in the crossstream and vertical velocities. The evolution  $v$  and  $w$  dictated, is represented in the second row ((e)-(h)) for  $v$  and in the third row ((i)-(l)) for  $w$  in the upper (lower) rotor part (Fig. ??(a)). As predicted by the analysis of Sect. 3 (Eq. 15), the signs of  $v$  are opposite in the upper and the lower rotor half for CR and CCR, respectively (compare Fig. ??(a)), in comparison to the northward (southward) deflected one in  $NV\_CCW$  (Fig. ??(b)) (5(e) to (g) and (f) to (h)). The same is valid for the signs of  $w$  (Eq. 10) (compare Fig. ??(b)) (i) to (k) and (j) to (l)). The change in the deflection from northward to southward and vice-versa results from the interaction of a clockwise blade rotation with the veered inflow conditions. (5(i) to (k) and (j) to (l)). This difference between CR and CCR is pronounced at



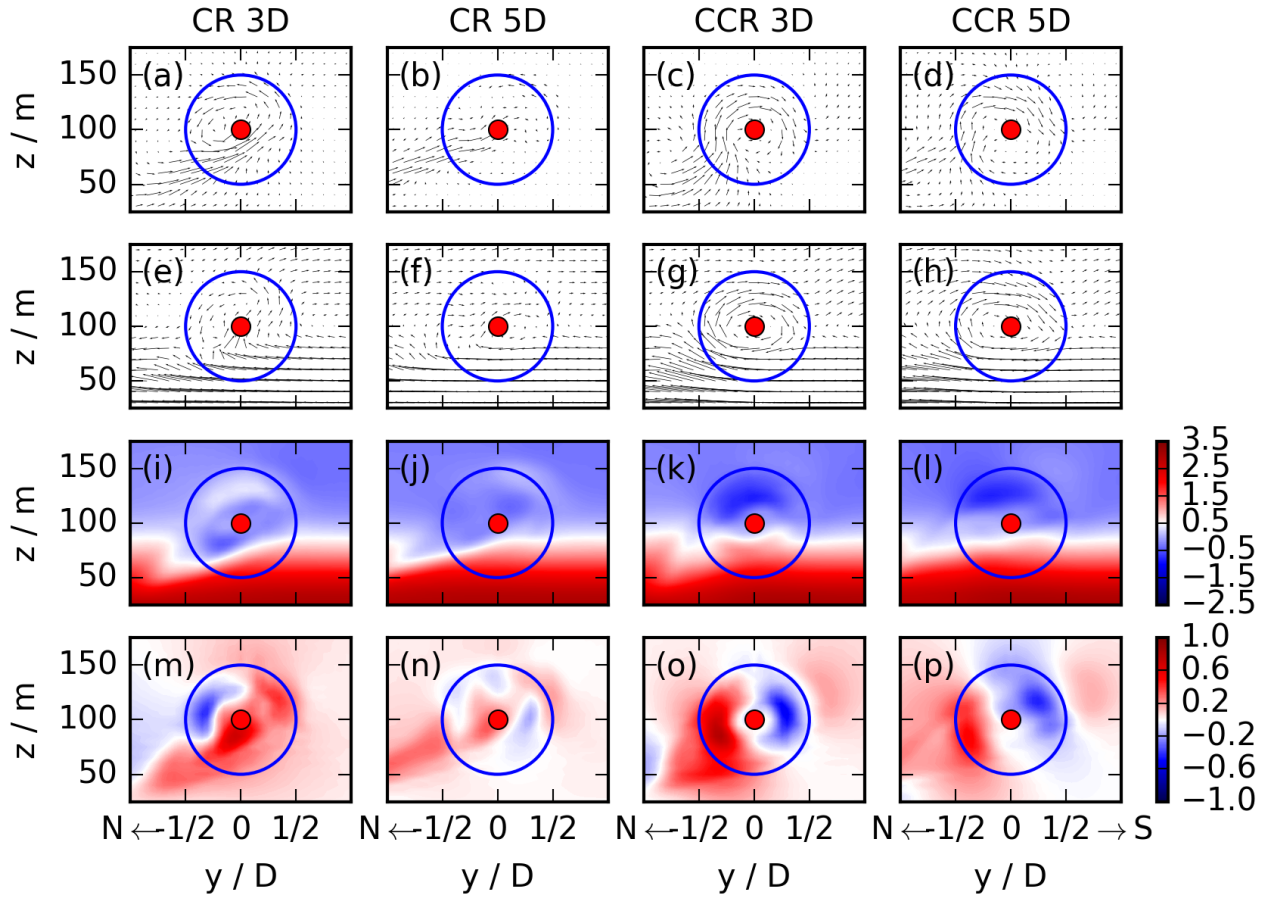


**Figure 6.**  $y$ - $z$ -cross sections of the SBL wind-turbine simulations for CR and CCR at  $x=3D$  and  $5D$ . The first row ((a)-(d)) presents the  $(v, w)$  vectors as difference between the vector at  $x=3D$  (or  $5D$ ) and the inflow region, the second row ((e)-(h)) represents the velocity vector in the  $y$ - $z$ -plane, the third row ((i)-(l)) the meridional wake velocity  $v$ , and the fourth row ((m)-(p)) the vertical wake velocity  $w$ . The blue contour represents the circumference of the actuator. The streamwise flow is from the west and these cross sections correspond to a view towards the east downwind through the turbine with north on the left and south on the right.

a downwind distance of  $x=3D$ . At  $x=5D$ , the difference is smaller as  $v$  and  $w$  approach the inflow conditions of  $\approx 0 \text{ m s}^{-1}$  (Fig. 3(a)).

To further investigate-

In contrast to the no veer case, the effect of wind-veer on counterclockwise rotating wind turbines, we compare  $V_{CW}$  and  $NV_{CW}$ , in Figs. ??(e) vs. (f), ??(e) vs. (f), and ??(e) vs. (f). The veering wind causes a more rapid wake recovery in the veering inflow on the top half of the rotor (Fig. ??(e) vs. wind-turbine wake will not be limited to the change of the sign, also the wake characteristics will be different in CR and CCR, as suggested by the analysis of Sect. 3. Figure 6 represents the wake characteristics for a veering inflow in the SBL wind-turbine simulations. Here, the top row ((a) - (d)) represents the  $(v, w)$  vectors in  $y-z$ -plane as difference between the quantities at  $x = 3 D$  (or  $5 D$ ) and upstream at  $x = -2 D$  to emphasize the effect of the rotating actuator. At a downwind distance of  $x = 3 D$ , the rotational direction of the rotor determines the wake rotation in both cases. Differences emerge by  $5 D$  downwind. The wake rotation in CCR is the same as at  $x = 3 D$ , but only the magnitude of the  $(v, w)$  vectors is smaller. In CR, however, the magnitude of  $(v, w)$  approaches zero and the rotational direction of the rotor no longer determines the wake rotation. Further, the applied vortex leads to an inflow into the lower northern rotor part, resulting in rising motion in the southern rotor part in CR (Fig. ??(f)) as well as in the bottom half of the rotor (6(a)), whereas it ascends in the northern rotor part in CCR (Fig. ??(e) vs. 6(c)).

The second row (Fig. ??(f)) - In contrast to  $V_{CCW}$  vs.  $NV_{CCW}$  (6(e) - (h)) corresponds to the first row of Fig. ??(a) vs. 5, representing the vectors  $(v, w)$  at  $x = 3 D$  and  $5 D$ . The magnitude is weaker in CR (Fig. ??(b)), the wake recovers much more rapidly in  $V_{CW}$  (6(e)) in the upper and lower rotor part in comparison to CCR (Fig. ??(e)) in comparison to  $NV_{CW}$  (6(g)), resulting in larger and more organised  $(v, w)$  wind components in CCR. At a downwind distance of  $x = 5 D$ , in CCR (Fig. ??(f)(h)), especially in the far wake. The veering wind further impacts the wake deflection angle. The wakes in the veered simulation  $V_{CW}$  as well as in the non-veered simulation  $NV_{CW}$  are deflected towards the south (north) the rotational direction of the wake flow is the same as at  $x = 3 D$ , only the strength is weaker. In case of CR (Fig. 6(f)), however, the flow direction in the upper (lower) rotor part with a larger wake deflection angle in  $V_{CW}$  rotor half has changed in comparison to  $x = 3 D$  (Fig. ??(e), (f)(Fig. ??(e), (f))). The same northward wake deflection in - Now it flows from north to south, resulting in a wake which is clearly dominated by the inflow.

To distinguish both contributing parameters of the  $(v, w)$  vectors, the upper  $v$ -cross sections are presented in the third row ((i) - (l)) of Fig. 6. The positive and negative perturbations in  $v$  are the opposite in CR (Fig. ??(e), (f)) and the same southward wake deflection in the lower (6(i)) and CCR (Fig. 6(k)) in the corresponding rotor sector at  $x = 3 D$ , with larger  $|v|$  values in the upper and lower rotor sector in case of CCR. This pattern is weakening downwind and persists at  $x = 5 D$  (Fig. ??(e), (f)) rotor part for  $V_{CW}$  and  $NV_{CW}$  result from the interaction of a counterclockwise blade rotation with veered and non-veered inflow conditions. It contrasts the changes in height in the wake deflection from northward to southward in  $V_{CCW}$  (6(j), (l)).

Considering the  $w$ -cross section in the fourth row ((m) - (p)) of Fig. ??(a) vs. 6, the upward and downward orientation of  $w$  differs at  $x = 3 D$  (Fig. 6(m), (o)) in the northern and the southern sector and also for CR (Fig. ??(a)(m)) and vice versa in  $NV_{CCW}$  - CCR (Fig. ??(b) vs. 6(o)) comparing the same sectors. In comparison to the EBL wind-turbine simulations (Fig. ??(b)). Further, the wake width in the far wake differs, especially at hub height 5(i) - (l), the veering inflow has an additional effect on the vertical velocity in the wake at  $x = 3 D$  (Fig. ??(e), (f)(m) and (o)). As this is not the case in  $V_{CCW}$  vs.  $NV_{CCW}$  (The veering inflow leads to an intensified wake entrainment at the lower northern rotor part, which is independent of the rotational direction (see inflow pattern of the  $(v, w)$  vectors in the lower northern rotor part in Fig. ??(a) vs. (b)),

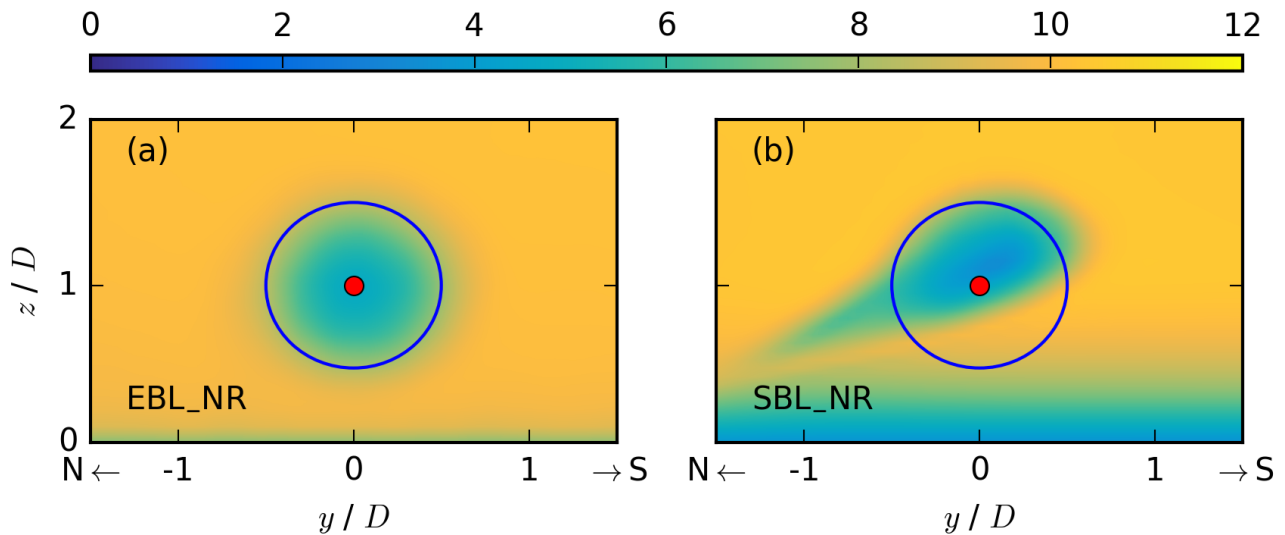


**Figure 7.** Coloured contours of the time averaged zonal velocity  $\overline{u_{i^*,j,k}}$  in  $\text{m s}^{-1}$  at a downward position of  $x = 5 D$  with index  $i^*$  behind the rotor of the non-rotating EBL wind-turbine simulation without wind veer in (a) and the non-rotating SBL wind-turbine simulation with veering inflow in (b). The blue contour represents the circumference of the actuator.

it is also an effect of the interaction of counterclockwise rotating blades with a veering wind. In summary, the differences between the veered and the corresponding non-veered simulations are much larger for a clockwise wake rotation and (c). At this location the flow is directed upward. In case of CCR, it overlaps with the updraft in the northern sector, resulting in a rising motion of  $w$  in the northern part at  $x = 3 D$  (Fig. ??(e) vs. 6(o)). In case of CR, a new updraft region manifests, weakening the downward region in the northern rotor part. This interaction results in an updraft in the southern rotor part at  $x = 3 D$  (Fig. ??(f)) in comparison to a counterclockwise one 6(m)). At  $x = 5 D$  (Fig. ??(a) vs. Fig. ??(b)) 6(n), (p)), the flow pattern is the same as at  $x = 3 D$ , only the strength is weaker.

As an intermediate step

#### 4.2 Impact on streamwise velocity and total turbulence intensity

The rotational direction of the rotor modifies the spanwise and vertical velocity components in the wake under veering inflow. Here, we investigate the rotational effect under veered inflow conditions by comparing V\_CCW with V\_NR. The veered inflow condition in combination with clockwise rotating blades results in a more rapid flow recovery in the near wake and a less rapid one in the far wake at hub height in V\_CCW their effect on the streamwise velocity and the total turbulence intensity.

The inflow profiles from Fig. 3(a) predict a different wake behaviour under veering inflow in comparison to no wind veer, regardless of the rotational direction. Therefore, different wake characteristics should prevail in both non-rotating simulations

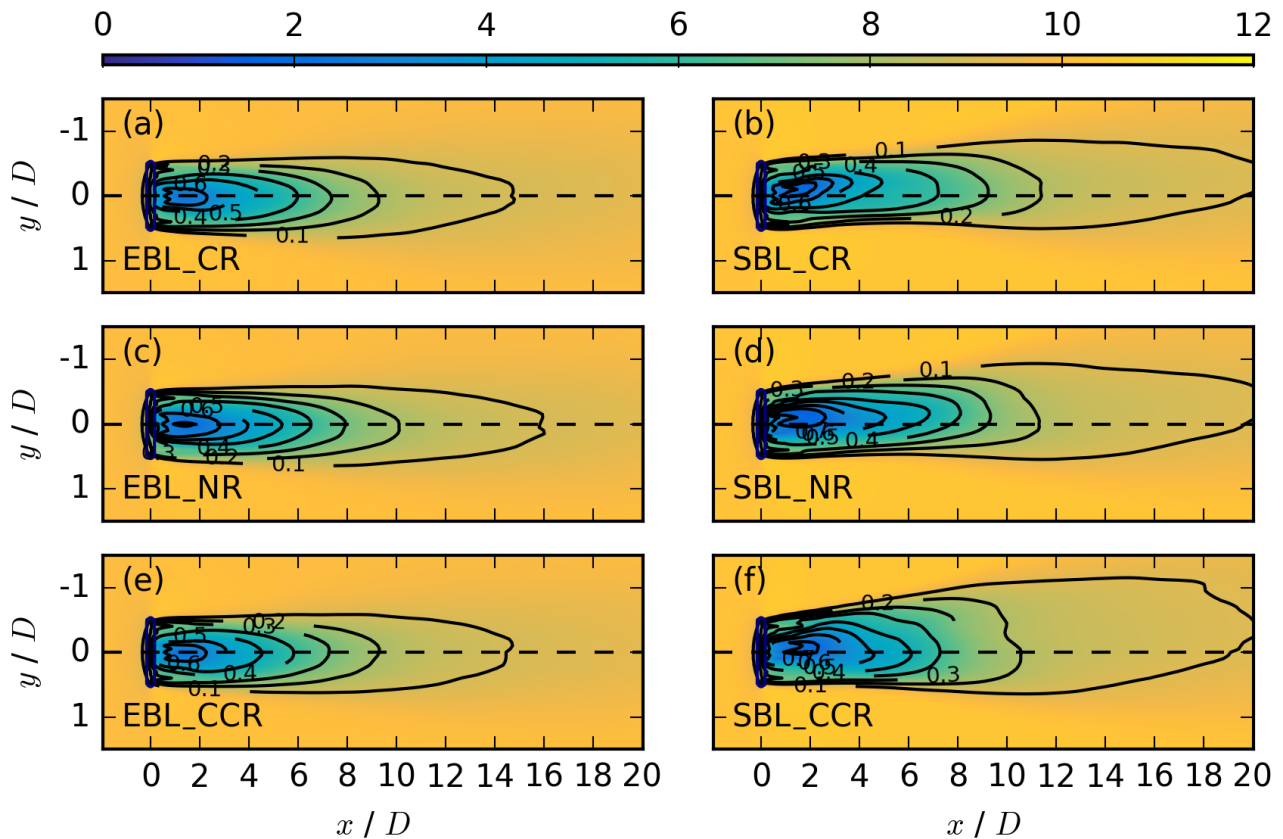


**Figure 8.** Coloured contours of the streamwise velocity  $\overline{u_{i,j,k_h}}$  in  $\text{m s}^{-1}$  at hub height  $k_h$ , averaged over the last 50 min, for EBL\_CR in (a), SBL\_CR in (b), EBL\_NR in (c), SBL\_NR in (d), EBL\_CCR in (e), and SBL\_CCR in (f). The black contours represent the velocity deficit  $VD_{i,j,k_h}$  at the same vertical location.

NR. Figure 7 represents  $y$ - $z$ -cross sections of the streamwise velocity at  $x = 5 D$  for the non-rotating wind-turbine simulations with a non-veered inflow in the evening in (a) and a veering inflow in a stable regime in (b). In case of no veer, the wake at  $x = 5 D$  retains the shape of the rotor (Fig. ??7(a)) in comparison to  $V_{\text{NR}}$ . In the case of a veering inflow, the wake in the lower rotor half shifts to the north (Fig. ??(e7(b))). Defining a wake deflection angle of zero for a non-deflected wake, the combination of veered inflow conditions and clockwise disc rotation reduces the wake deflection angle in the top-tip (The striking difference in the lower rotor part corresponds to the inflow profiles of Fig. 3(a), where a veering inflow is characterized by a southern component for  $z < 100 \text{ m}$  in the SBL, whereas the meridional inflow velocity is  $\approx 0 \text{ m s}^{-1}$  in the EBL in all rotor heights. The skewed wake is only due to the veering inflow, as it also occurs without a rotating rotor. This simulated structure resembles those of the simulations of Abkar and Porté-Agel (2016), Vollmer et al. (2017), Bromm et al. (2017), Churchfield and Srinivas (2018) and Englberger and Dörnbrack (2018a).

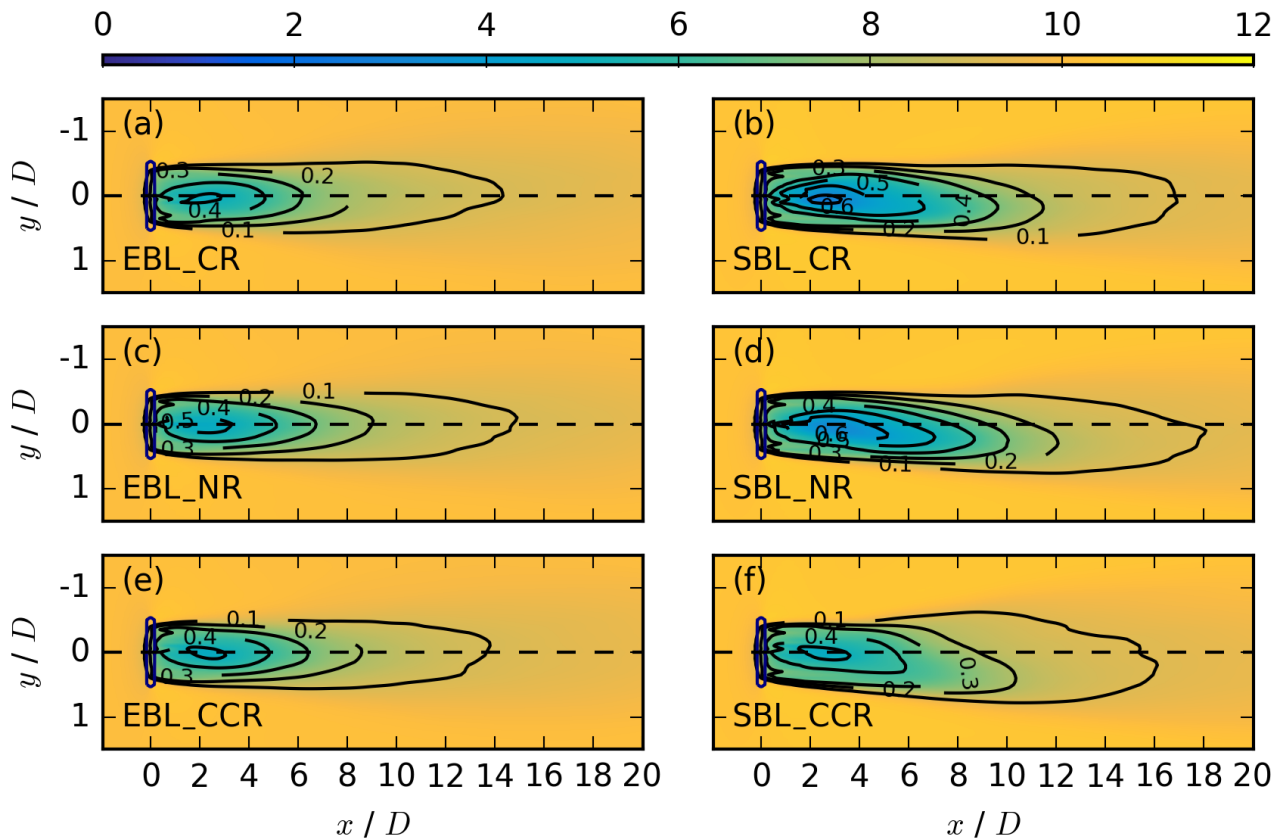


**Figure 9.** Coloured contours of the streamwise velocity  $\overline{u_{i,j,k_*}}$  in  $\text{m s}^{-1}$  at  $z_h = 125$  m with index  $k_*$ , averaged over the last 50 min, for the same cases as in Fig. 8. The black contours represent the velocity deficit  $VD_{i,j,k_*}$  at the same vertical location.

The evolution of the wake at specific altitudes also show the effect of veer. The streamwise velocity appears at hub height of  $z_h = 100$  m in Fig. 8, in the upper rotor part at  $z = 125$  m in Fig. ??(a)) and the bottom tip sectors (9 and in the lower rotor part at  $z = 75$  m in Fig. ??10 for the EBL (no veer) wind-turbine simulations in the left column ((a)) in V\_CCW in comparison to V\_NR (Figs. ??(e), ??(e)). Both effects arise from a clockwise blade rotation, (c), (e) and the SBL (veered) wind-turbine simulations in the right column ((b), (d), (f)) for a clockwise rotating rotor CR in the first row, no rotation of the disc NR in the second row, and a counterclockwise rotating rotor CCR in the third row.

To further investigate the impact of the rotational direction, we also compare V\_CW to V\_NR. Here, a more rapid wake recovery persists in the whole wake in V\_CW. According to the analysis of Sect. 3, disregarding the sign in Eq. 17, no significant wake differences are expected in the non-veering simulations of the EBL for CR and CCR. This is in agreement with the situation at hub height (Fig. ??(e8(a) vs. Fig. ??(e(e)). Further, counterclockwise rotating blades increase the wake deflection angle in the top tip (Fig. ??(e)) and the bottom tip sectors (Fig. ??(e)) in V\_CW in comparison to V\_NR. Above and below

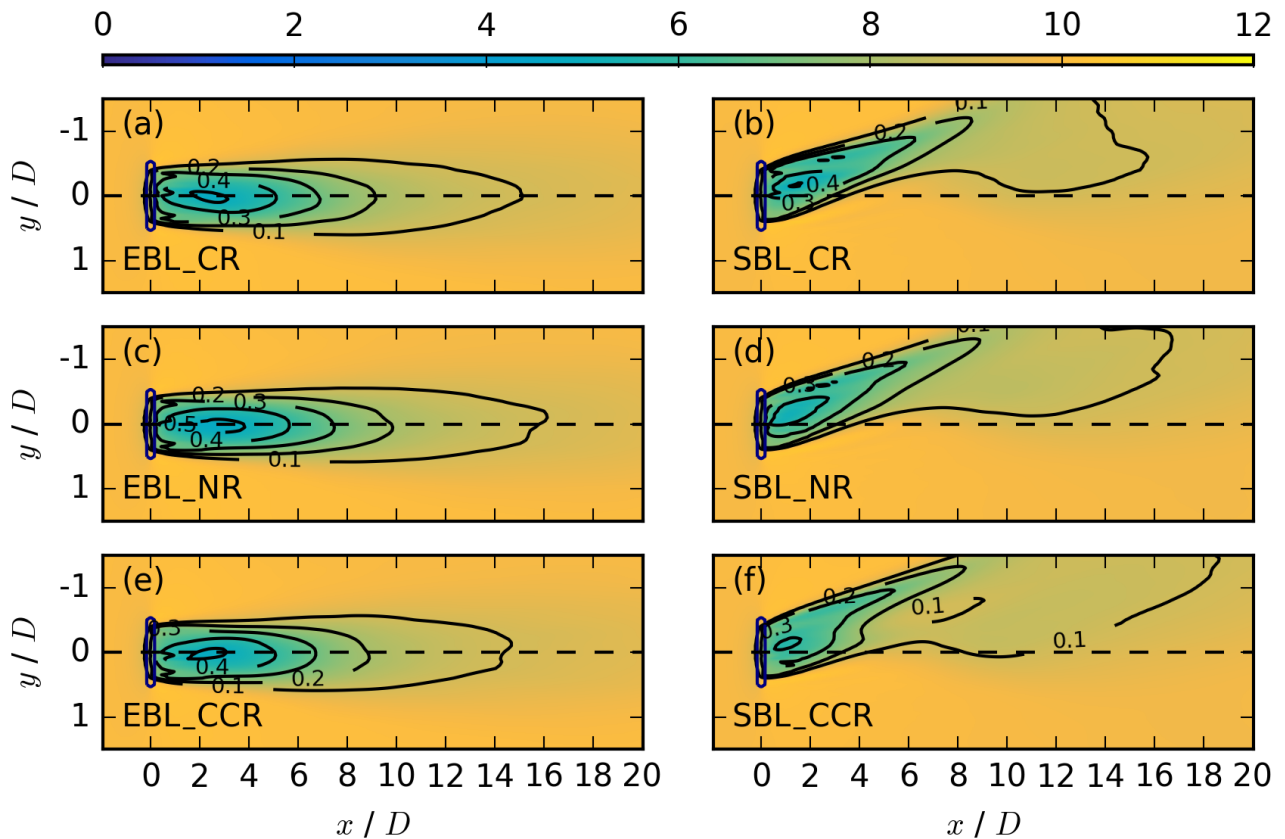


**Figure 10.** Coloured contours of the streamwise velocity  $\overline{u_{i,j,k_*}}$  in  $\text{m s}^{-1}$  at  $z=75$  m with index  $k_*$ , averaged over the last 50 min, for the same cases as in Fig. 8. The black contours represent the velocity deficit  $VD_{i,j,k_*}$  at the same vertical location.

hub height, differences emerge in the near wake (Figs. 9(a), 9(e)), and likewise especially in comparison to V\_CW (Figs. 9(e), 10(a), 9(a)):

Therefore, the direct comparison of V\_CW and V\_CW (Figs. 9(e) vs. (a), 9(e) vs. (e)), resulting from the opposite sign in CR and CCR in the upper and lower rotor part (Eq. 17). The near wake deflects towards the north in the upper rotor half (Fig. 9(a), and 9(e) vs.) and towards the south in the lower rotor half (Fig. 10(a)) reveals that the wake recovery, the wake deflection angle, and the wake width depend on the rotational direction of the wind turbine. In V\_CW, the wake recovers more rapidly in CR, whereas it deflects towards the north in the lower rotor part (Fig. 10(e) vs. (a)) and the wake deflection angle is much larger) and towards the south in the upper rotor part (Fig. 9(e)) in CCR. In contrast, the non-rotating EBL simulation NR does not show any near wake deflection at any height (Figs. 9(e) vs. (a), 9(e) vs. (a)) in comparison to V\_CW. Further, the wake width is larger spanwise in V\_CW (8(c) - 10(c)). The effect in the rotating actuator simulations is therefore caused by the

rotation of the rotor, and can be explained by a transport of higher momentum air counterclockwise (clockwise) in CR (CCR), with the opposite situation prevailing at 75 m.

Wake elongation also exhibits the impact of the rotor's rotation. Comparing NR to CCR and CR of the EBL regime, there is further a difference in the wake elongation, with a larger velocity deficit in NR at hub height (Fig. 8(c)) at the same downwind position in comparison to V\_CCW CCR and CR (Fig. ??8(e) vs. and (a)). The faster recovery is related to enhanced entrainment in the CR and CCR simulations as the rotation itself acts as source of turbulence.

In comparison, in the non-veered simulations NV\_CCW and NV\_CW, the impact of the rotational direction on the wake recovery is very limited in the near wake and slightly increases in the far wake case of a veering inflow, the analysis of Sect. 3 predicts significant wake differences in the CR and CCR wind-turbine simulations of the SBL regime, which are not limited to the change of the sign in CR and CCR. The wake structures at hub height, presented in Fig. ??8(b) vs. and (d) for the CR and the NR simulations are comparable regarding the elongation, the width, and the deflection angle, respectively. The wake structure in CCR (Fig. 8(f)). The impact on the wake deflection angle results from the rotational direction of the wake and is nearly axis-symmetric in the near wake (Figs. ?? differs. Considering the black velocity deficit contours (Eq. 4), the wake recovers more rapidly and, especially in the far wake, it is broader with a slightly larger wake deflection angle towards the dashed center line.

The same situation occurs in the upper rotor part at 125 m (Fig. 9). Under veering wind conditions, the wake characteristics are also comparable in CR (Fig. 9(b) vs. (f) and ??(b) vs. ) and NR (Fig. 9(d)), with a slightly less rapid wake recovery in NR due to no additional turbulence generated by disc rotation. Comparing CR (and NR) to CCR (Fig. 9(f)). These differences in the non-veered simulations are in agreement with Vermeer et al. (2003), Shen et al. (2007), Sande (2009), Kumar et al. (2013), Hu et al. (2013), Yuan et al. (2014) and Mühle et al. (2017). However, compared to the rotational direction impact under veered inflow conditions, they can be considered of minor importance for a possible downwind turbine.

Therefore, the differences in the streamwise elongation of the wake, the spanwise wake width, and, the wake recovers much more rapidly in CCR, with a smaller velocity deficit in the near wake with  $VD_{max} \approx 0.4$  in comparison to  $VD_{max} \approx 0.6$  in CR and NR. A comparison of NR EBL (Fig. 9(c)) to NR SBL (Fig. 9(d)) shows a wake deflection angle in the NR SBL simulation, resulting from a meridional wind component  $\leq 0 \text{ m s}^{-1}$  in the upper rotor part (Fig. 3(a)). Comparing the rotating SBL cases (Fig. 9(b), (f) to NR (Fig. 9(d)), the wake deflection angle between V\_CW and V\_CCW are a superposition effect of wind veer and clockwise wake rotation, as they do not occur to the same extent for a counterclockwise wake rotation in combination with the same veered inflow conditions. Further, the differences do not occur at all under non-veered inflow conditions, independent of the rotational direction. The responsible mechanism behind this striking difference in the streamwise velocity profiles for the combination of veered inflow conditions with counterclockwise rotating blades in comparison to clockwise rotating blades will be evaluated in more detail below.

decreases in CR, whereas it increases in CCR. This deflection results from the counterclockwise transport of higher momentum air in CR and the clockwise transport in CCR. Interestingly, although veer is constrained to the lower half of the rotor disk, these differences in the upper half of the wake still occur.



Variations in these wakes also occur in the cross-stream  $v$  and vertical wind  $w$  components. Figure ?? represents the flow fields of  $v$  and  $w$  at 3D, 5D and 7D for the three veered cases. According to the analysis of Sect. 3, the effect of the rotational direction on  $v$  and  $w$  at 3D, 5D and 7D for the three veered cases. At 3D, the flow field in the rotor region of V\_NR is predicted to be much larger in the lower rotor part, and this is also expected for  $u$ . Figure 10(b), (d), and (f) represent the situation in the lower rotor part at 75 m. CR (Fig. ??10(b)) is only determined by the boundary-layer flow which is decelerated due to the interaction with the rotor. The flow field in the rotor region in V\_CW and NR (Fig. ??(e)) shows the same rotational direction as the boundary-layer flow. The interaction of both flow fields results in an intensified rotation in the rotor region. V\_CCW shows the opposite rotational direction of the flow field in the rotor region in comparison to the boundary-layer flow 10(d) again show similar wakes, however, comparing CR (and NR) to CCR (Fig. ??(a)). The interaction weakens the rotor-induced rotation in the rotor region. The strength of the rotational direction in the rotor region is therefore weaker in V\_CCW in comparison to V\_CW 10(f), the velocity deficit maximum, the elongation, the width, and the deflection angle of the wakes differ. Compared to the difference in the wake deflection angle in the near wake for CR and CCR in the EBL wind-turbine simulations (Fig. ??10(a) vs. (e)). At 5D, the rotational direction in V\_CW is the same as at 3D and (e), the wake deflection angle in the SBL wind-turbine simulations (Fig. ??(f) vs. (e)), with a comparable strength of the  $v$  and  $w$  flow fields and likewise of the rotational direction. In V\_CCW, the rotation of the flow field induced by the rotor disappears and the rotation of the boundary-layer flow now dominates 10(b) and (f) is also influenced by the inflow wind direction angle. In case of CR, the wake deflection angle decreases (Fig. ??(d) vs. (a)). At 7D, the flow rotation in the rotor region is the same in V\_CCW and V\_CW, with a much more pronounced rotation pattern in V\_CW 10(b)), whereas in CCR, it increases (Fig. ??(g) vs. (i)). In V\_CCW, the wind turning of the Ekman spiral emerges in the rotor region at 7D 10(f), similar as in the upper rotor part (Fig. ??(g)), an effect related to the overlapping of the veering wind in the boundary-layer flow with an opposite directed flow rotation induced by the rotor 9(b) and (f).

In contrast, the non-veered cases are represented in For a more qualitative investigation of the impact of the rotational direction on the wake under veering inflow, Fig. ??, also for the flow fields of  $v$  and  $w$  and at 11 shows vertical and spanwise profiles through the rotor center of the streamwise velocity in the first two rows ((a) - (h)) and also of the total turbulence intensity (Eq. 6) in the last two rows ((i) - (p)) at  $x = 3D, 5D$  and  $7D$ . At  $3, 5$  and  $10D$ , the flow field in the rotor region of NV\_NR (Fig. ??(b)) is again only determined by the boundary-layer flow, with  $v_{BL}(z)$  for CR and CCR rotating turbines in the SBL (solid red (CR) and blue (CCR) lines) and the EBL (dashed red (CR) and blue (CCR) lines).

Without veering inflow, the difference in  $u$  and  $TI$  between CR and CCR is trivial. Further, the profiles are almost symmetric to the rotor center lines of  $z = 0$  and  $w_{BL}(z)$  and  $y = 0$ , and the deceleration due to the interaction with the rotor. The arising pattern is related to the flow deceleration of the non-rotating disc. NV\_CCW-D. However, under veering wind conditions in the SBL, significant differences emerge. Considering the upper rotor part up to  $z = 150$  m in the vertical profiles of  $u$  (Fig. ??11(a)) and NV\_CW - (d) and  $TI$  (Fig. ??(e)) are axis-symmetric to each other. Here the strength of the rotational direction is the same in both simulations, as it is only determined by the tangential force imposed by the wind-turbine parametrization  $F_{\Theta}$  in Eq. (1). The opposite rotational direction is related to the opposite sign of  $\beta_v$  and  $\beta_w$ . The axis-symmetric structure persists up to 11(i) - (l), the downwind velocity in case of CCR is larger in comparison to CR, whereas the total turbulence intensity is larger up to  $x = 7D$  downstream (Fig. ??(d), (g) vs. (f), (i)).



## 5 Simplified Wake Model

The streamwise recovery of the wake, the spanwise wake width, and the wake deflection angle differ between V\_CCW and V\_CW, while these differences do not emerge in the non-veered cases NV\_CCW and NV\_CW. The flow fields of  $v$  and  $w$  differ between V\_CCW and V\_CW, whereas  $v$  and  $w$  are axisymmetric in NV\_CCW and NV\_CW. The different behaviour of V\_CW and smaller at  $x = 10D$ . In the top-tip region of the rotor and for  $z \geq 150$  m, the total turbulence intensity is larger in case of CR in comparison to V\_CCW arises from the interaction of the Ekman spiral in the boundary-layer flow with the clockwise flow rotation induced by the counterclockwise rotating rotor.

### 4.1 Model Development

To demonstrate this interaction and the difference between V\_CW and V\_CCW, we introduce a simplified wake model, which is a linear superposition of the atmospheric boundary-layer flow  $u_{BL}$ ,  $v_{BL}$ , and  $w_{BL}$  (Equations , , and ) with a wind-turbine model. The wind-turbine model includes the axial turbine-induced force  $\mathbf{F}_x$ , as well as the tangential turbine-induced force  $\mathbf{F}_\Theta$ , which correspond to a Rankine Vortex (Lamb, 1993)

$$\begin{aligned} 3u_{WT} &= 0.3 \cdot u_{BL} \\ v_{WT} &= v_{RV} = \pm \omega r \frac{r}{R} \cos(\Theta) \\ 15 \quad w_{WT} &= w_{RV} = \mp \omega r \frac{r}{R} \sin(\Theta), \end{aligned}$$

with  $\omega$  representing the angular velocity of the flow induced by the angular velocity of the wind turbine  $\Omega$ ,  $r$ , and  $\Theta$  correspond to the position in the disc region and  $R$  to the rotor radius. Equation is motivated by CCR for  $x \geq 5D$ . To investigate the impact in the lower rotor part, a vertical profile through the rotor center is not appropriate due to wake deflection. Therefore, spanwise profiles of  $u$  and  $TI$  at 75 m are shown in the first ((a)-(d)) and third ((i)-(l)) row of Fig. ???. Here, the flow is not completely decelerated directly behind the disc,  $u(\text{rotor}) > 0$ , including the deflected wake towards the north at  $y > 0$ , as in EULAG the rotor of a wind turbine is not implemented as a real circular obstacle (e. g. grid-point blocking as in Heimann et al. (2011)). Instead, at every grid point covered by the rotor  $D$ . Up to at least  $x = 7D$  (Fig. 12(a)-(c)), the streamwise velocity field experiences the turbine-induced force  $\mathbf{F}_x$  according to Eq. 1. This implementation is inspired by the immersed boundary method (Smolarkiewicz and Winter, 2010). Considering this, the wind-turbine model includes a certain fraction of  $u_{BL}$  in  $u_{WT}$ . We apply a fraction of 0.3, which can be related to  $VD_{max}$  in the deflected wake is larger in the CCR case in the southern rotor part with a minor difference between CR and CCR and slightly larger values in CR in the northern rotor part, whereas differences between the profiles have eroded by  $x = 0.7$  of the rotating disc simulations in 10D (Fig. ??).

From a linear superposition results for the developed simplified wake model:-

$$\begin{aligned} 3u_M &= u_{BL} + u_{WT} \\ 30 \quad v_M &= v_{BL} \pm v_{WT} \\ w_M &= \pm w_{WT} \end{aligned}$$

and inserting Equations (12), (13), and (14) into Equation (11), a wake model arises, which depends on the radial position of the wake  $r$  (Equation (12)).

The lateral position  $y_*$  of the wake  $r$ :

$$\underline{3u_M(r)} = 1.3 \cdot u_g \cdot \left( 1 - \exp\left(-\frac{z\sqrt{f/\kappa}}{\sqrt{2}}\right) \right)$$

$$\underline{v_M(r)} = \tan\left(\left(270^\circ - \left(262^\circ + 8^\circ \frac{z}{100m}\right)\right) \frac{\pi}{180^\circ}\right) \cdot u_g \cdot \left( 1 - \exp\left(-\frac{z\sqrt{f/\kappa}}{\sqrt{2}}\right) \right) \pm (\pm\omega r \frac{r}{R} \cos(\Theta))$$

$$5 \quad \underline{w_M(r)} = \pm(\mp\omega r \frac{r}{R} \sin(\Theta))$$

Two effects need to be considered in the model: The position of the complete wake recovery  $x_{rec}$  with  $u(x_{rec})$  center at  $x = 3 D_{BL}$  in relation to each downstream position  $x_{pos}$  ( $x_{rec} = 5 D, 7 D, 20 D$  and  $10 D$  at  $z = 75$  m is shown in Fig. 10(b) for CR and in Fig. 10(f) for CCR. In case of CCR at  $x = D$  according to Figures (10), (11), and (12). The downstream erosion of  $v_{WT}$  and  $w_{WT}$  with  $x_{fad}$  corresponding to a prescribed decay distance at which the atmospheric boundary-layer flow determines the rotational direction of the wake ( $3 D < x_{fad} < 5 D, y_* = D$  according to Figure (10))  $\approx -1/2 D$  and at  $x = 7 D, y_* \approx -1 D$ , with slightly smaller values of  $y_*$  in case of CR, resulting from the smaller wake deflection angle in CR in comparison to CCR (compare Fig. 10(b) to (f)). Therefore, comparing  $u$  at the corresponding wake center positions in Fig. 12(a)-(d),  $u_{CCR} > u_{CR}$  for  $x < 10 D$ . In Equations (11)-(14), we prescribe a simplified wake model, which depends on the radial position of the wake  $r$  and also on the downwind position  $x_{pos}$ :

$$\underline{3u_M(r, x_{pos})} = 1.3 \cdot u_g \cdot \left( 1 - \exp\left(-\frac{z\sqrt{f/\kappa}}{\sqrt{2}}\right) \right) \cdot \left(\frac{x_{pos}}{x_{rec}}\right)^\gamma$$

$$\underline{v_M(r, x_{pos})} = \left( v_{BL} \pm (\pm\omega r \frac{r}{R} \cos(\Theta)) \left(\frac{1}{\exp\left(\frac{x_{pos}}{x_{fad}}\right)}\right)^\delta \right) \cdot \left(\frac{x_{pos}}{x_{rec}}\right)^\gamma$$

$$\underline{w_M(r, x_{pos})} = \pm(\mp\omega r \frac{r}{R} \sin(\Theta)) \cdot \left(\frac{1}{\exp\left(\frac{x_{pos}}{x_{fad}}\right)}\right)^\delta \cdot \left(\frac{x_{pos}}{x_{rec}}\right)^\gamma,$$

with  $\delta$  describing the entrainment of ambient air into the wake and  $\gamma$  the wake recovery where the difference also decreases downwind.

Sector averages of  $u$  in (a),  $v$  in (c), and  $w$  in (e) for the veered cases V\_CCW and V\_CW.  $u$  and  $v$  show the top-tip and bottom-tip sectors,  $w$  the right (solid line) and left (dashed line) sectors. The corresponding model components are shown in (b) for  $u$ , (d) for  $v$ , and (f) for  $w$ .

#### 4.1 Comparison with Simulation Results

25 This simplified model is able to capture the observed behaviour of the LESs. Figure (11) compares the results of the veered simulations V\_CCW and V\_CW to this simplified wake model (Equations (11)-(14)). Contrasts in turbulence intensity emerge, due to differences in entrainment. The total turbulence intensity around  $y = 0 D$  in the lower rotor part (Fig. 12(i) - (j)). The left panel

shows the sector-averaged velocity values of  $u$  and  $v$  of the top-tip and (l) shows the bottom-tip sectors. The velocity values of  $w$  correspond to the right and the left sectors, also for both rotational directions. In the simplified wake model, we apply the parameters same relation between CR and CCR as in the upper rotor part (Fig. 12(m) = 145 m and  $\Theta(p)$ ) and at hub height (Fig. 11(m) - (p)), with  $TI_{CCR} > TI_{CR}$  up to  $x = 0^\circ$  for the top-tip sector, and 7 D. However, considering the difference in the deflected wake at  $z = 55$  m and  $\Theta 75^\circ$  m ((j) =  $-180^\circ$  for the bottom-tip sector as well as  $\Theta(l)$ ),  $TI_{CCR} \leq 90^\circ$  for the right sector and  $\Theta TI_{CR}$  at  $x = 270^\circ$  for the left sector. Further,  $u_{q3} = D$  for  $y 10 \text{ m s}^{-1}$ ,  $\omega \leq y_* = 7 \text{ rpm}$ ,  $x_{rec} = 1/2 \text{ D}$  (Fig. 12(i)). Approaching downwind, the difference in  $TI$  between CR and CCR decreases for  $x > 5 \text{ D}$  (Fig. 12(j) - (l)). The much larger values of CCR at  $y = 250 \text{ D}$ ,  $x_{fad}$  in the lower rotor half for  $x \leq 47 \text{ D}$ ,  $\gamma = 0.4$ , and  $\delta = 2.5$ .

The main characteristics are very well represented by the simplified wake model, especially for the  $\bar{v}$  and  $\bar{w}$  components. It can reproduce the change of the flow rotation in the wake in CCW and the correct signs of  $\bar{v}$  and  $\bar{w}$  for both rotational directions.

In more detail, the simulation results (Fig. 12(i) - (k)) can be explained with a broader wake width approaching the center line in Fig. ??(a) show a larger zonal velocity in the top-tip sector, which is directly related to  $u_{BL}(tt) > u_{BL}(bt)$  in Eq. ??. This effect is represented by the simplified wake model in 10(f) in comparison to Fig. 10(b) representing CR. Approaching  $x = 10 \text{ D}$  (Fig. ??(b)). Further, the  $\bar{u}$ -values are larger in  $V_{CW}$  12(l)), the profiles for CR and CCR become rather similar, no longer showing a rotational direction impact. Larger  $TI$  values in CCR in comparison to  $V_{CCW}$ . This results from the interaction of  $u$  with  $v$  and  $w$ . The simplified wake model did not consider this interaction, leading to an overlap of both top-tip and bottom-tip sectors in Fig. ?? CR can be explained by a more rapid wake recovery (Figs. 8 and 10(f) vs. (b)). Further, in the simplified wake model, the zonal velocity values are smaller resulting from a larger entrainment rate in CCR in comparison to the simulation results. In addition to a different choice of the prefactor of 0.3 in  $u_{WT}$ , this magnitude can also be modified by the wake recovery parameter  $\gamma$ , where a smaller value results in larger zonal velocity values. CR.

The simulation behaviour of the meridional velocity  $\bar{v}$  in Fig. ??(c) differs depending on the rotational direction of the wake (CCW or CW). Firstly, Summarizing, the rotational direction has no significant impact on  $u$  and  $TI$  in the case of no wind veer, represented by our EBL simulation. However, in case of a veering wind in the opposite sign of  $\bar{v}_{SBL}$ , a consistent downwind impact on  $u$  and  $TI$  emerges at all heights over the rotor, with larger  $u$ -values prevails in both top-tip (bottom-tip) sectors in the near wake (as it is the case in the non-veered simulations (not shown here)). Secondly, an additional change of the sign in  $\bar{v}$  occurs only in CCW between 3 D and 4 D, a downstream position which is similar to  $x_{fad}$  in Fig. ??. The sign does not dominate if wind veer interacts with a clockwise rotating wake (CW). This interaction in the CCW case and  $TI$ -values in case of CCR in comparison to CR.

## 5 Comparison of a rotating wind turbine under veering inflow to analysis predictions

The striking difference between the wake characteristics of the no-veer EBL and the veering SBL wind-turbine simulations, and especially the difference between CR and CCR in case of a veering inflow, can be explained with the simplified wake model by a linear superposition of  $v_{BL}$  with  $v_{WT}$ . The downstream position of the change of the sign in  $v$  in the simplified

wake model for the counterclockwise case can be modified with the entrainment parameter  $\delta$ , whereas a larger  $\delta$ -value by the analysis of Sect. 3 with Eq. 17.

In the upper rotor part,  $v_f$  and  $v_v$  are the same in the EBL and the SBL wind-turbine simulations. In case of CR,  $|v_f| \approx 0$ , interacting with  $v_v$  flowing from south to north. As  $|v_v| \gg |v_f|$ , it results in a smaller downstream distance of the crossover as the impact of the boundary-layer flow on the wake sets in closer to the rotor. Further, the magnitude of  $v_M(r, x_{pos})$  agrees with the simulation results. This agreement is the reason why we did not choose a smaller  $\gamma$ -value to increase  $u_M(r, x_{pos})$ , as it would likewise increase the magnitude of  $v_M(r, x_{pos})$ . Thirdly, the magnitude of the  $\bar{v}$ -values is much smaller in the near wake in CCW in comparison to CW. In the far wake at  $x > 7D$ ,  $v$ -component flowing from south to north for the EBL in Fig. 5(e), (f) and the SBL in Fig. 6(i), (j). In case of CCR,  $v_v$  flows from north to south in the upper rotor part, resulting in a  $v$ -component also flowing from north to south for the EBL in Fig. 5(g), (h) and in the SBL in Fig. 6(k), (l).

In the lower rotor part,  $v_f$  differs in the EBL and the SBL regime (Fig. 3(a)). In case of no wind veer in the magnitude of  $\bar{v}$  is the same in both cases CCW and CW, as the rotational direction impact is marginal and the flow field is only determined by the Ekman spiral. The smaller  $\bar{v}$ -values in CCW result from the overlapping of a counterclockwise wake rotation with the Ekman spiral in EBL,  $v_f$  is the rotor region same over the whole rotor. Therefore, only the sign of  $v_v$  contributing to Eq. 17 changes in the lower rotor half, in comparison to the upper rotor half (Fig. ??(a)), whereas the overlapping of a clockwise rotating wake with the same Ekman spiral increases the  $\bar{v}$ -values in the near wake rotor region (Fig. ??(c)), both in comparison to x5(e), (f). Another effect of  $\frac{\partial v}{\partial z} \approx 70$  are the similar wake characteristics in panels (a) and (e) of Figs. 8 - 10. The only minor difference is the wake deflection angle in Figs. 9(a) vs. (e) and 10(a) vs. (e). The non-veering inflow also results in the symmetric structure to hub height and to  $y = 0D$  of  $u$  and  $TI$  in Figs. 11 and 12.

The simulation behaviour of the vertical component  $\bar{w}$  in the right and left sectors. In case of veering inflow,  $v_f > 0 \text{ m s}^{-1}$  in the lower rotor part and therefore flows from south to north. This pattern leads to a decrease of  $v$  in CR due to  $v_v < 0 \text{ m s}^{-1}$  (component from north to south) in Fig. ??(e) is determined by the downward transport of higher momentum air from above or the upward transport of lower momentum air from below. In V\_CCW (V\_CW), higher momentum air is transported downwards from the top-tip sector into the right (left) sector, resulting in negative vertical velocity 6(i), (j) and an increase in CCR due to  $v_v > 0 \text{ m s}^{-1}$  (component from south to north) in Fig. 6(k), (l). Further, the larger velocity deficit values in the right (left) sector. In CCW, the crossing of zero between 4 horizontal slides in Figs. 8 D and 5 D corresponds to the difference between 310 for (b) vs. (f) and the smaller  $u$ -values in the vertical and spanwise profiles up to at least  $x D$  and  $5 = 7D$  in the left and right sectors and to  $x_{fad}$  (Fig. ??). By changing the rotational direction, the positive and negative components change in both sectors. The crossing of zero occurs further downstream in CW due to the intensification of the boundary-layer flow and the rotational direction induced on the flow by the rotor. The general behaviour of positive and negative values can be represented with the simplified wake model in Fig. ??(f). As the only difference in the vertical component of the simplified wake model is the sign of  $w_{WT}$ , the curves for both rotational directions overlap. However, the crossing of zero is not represented, as this effect is not only a linear superposition effect.

Further, the main patterns of the simplified wake model for the non-veered case also agree with the simulation results of NV\_CCW and NV\_CW. The results are not shown in the scope of this work, however, they are straightforward with the only

difference of  $v_{BL}$  Figs. 11(a)-(d) and 12(a)-(h) in CR in comparison to CCR can be related to the reduction of  $v$  in the near wake in CR. Approaching downwind, the wake flow approaches the inflow conditions  $u_f$ ,  $v_f$ , and  $w_f$  at  $x_{down} = 0$  in Eq. 1.

## 6 Impact of Rotational Direction on the Flow in the Wake

The simplified wakemodel was introduced to explain the interaction between the incoming veering wind and opposite rotational directions by simple physics. The  $x_\xi > 20D$  in Figs. 8 - 10 for (b) and (f), as the contribution of  $v_v$  decreases according to analysis.

The behaviour of the total turbulence intensities (Figs. 11 and 12(i) - (p)) can also be explained by the analysis of Sect. 3. Smaller turbulence intensity values for CR in comparison to CCR can be related to a larger entrainment rate due to  $|v| > |v_f|$  in CCR, whereas,  $|v| < |v_f|$  in CR. Moving downwind to  $x = 10D$  (Figs. 11 and 12(l), (p)), the difference between the flow structure in the wake of simulation pairs V\_CCW and V\_CW and likewise the absence of this difference in NV\_CCW and NV\_CW could be explained by a simple linear superposition of  $v_{BL}$  with  $v_{WT}$ . The superposition represents the linear interaction of the rotor-induced vorticity with the vertical shear of the stably stratified. Between  $v$  and  $v_f$  decreases, resulting in similar values of  $TI$  for CR and CCR.

The resulting flow structures in the wakes are sketched. For a direct comparison of the stratified wind-turbine simulations of Sect. 4 with the analysis from Sect. 5, Fig. 13 compares averaged values for the sectors, as sketched in Fig. 2, of all simulated velocity components  $u$ ,  $v$ , and  $w$  up to  $x = 10D$  downwind for the no-veer EBL wind-turbine simulations in the left column and the veering SBL wind-turbine simulations in the right column. We start with a comparison of the non-veered case. The  $v$ -component of the EBL situation in Fig. 13(c) with  $v_f \approx 0 \text{ m s}^{-1}$  is comparable to the non-veering case A and Fig. 4(a). In the near wake, the vortex impact leads to a maximum of  $v$ . Approaching downwind, the impact of the rotor decreases, approaching to  $v_f \approx 0 \text{ m s}^{-1}$  at  $x_\xi \approx 7D$ . The only difference to the analysis in Fig. 4(a) is the linear behaviour of  $v$  in the near wake up to  $x = 3D$ , whereas the approximately linear decrease up to  $x = 7D$  is comparable. This near-wake difference results from the complex entrainment process in a turbulent atmospheric boundary layer, which is not considered in the analysis chapter. The behaviour of  $w$  of the EBL wind-turbine simulations in Fig. 1. In the cases without wind veer but with blade rotation, NV\_CCW and NV\_CW (13(e) shows the same characteristics as  $v$  in Fig. 1(b), (f)), the rotational direction of the flow impressed by the corresponding blade rotation persists through the whole wake with decreasing strength as the 13(c), only for the southern (solid line) and northern (dashed line) sectors. Therefore, the behaviour of  $v$  and  $w$  corresponds to the expected results from Eqs. 9 and 10. The  $u$ -values of the EBL wind-turbine simulations in Fig. 13(a) are constant up to  $x = 3D$ , followed by a linear increase which flattens at approximately  $x = 7D$ . This downwind evolution is comparable to the  $v$  and  $w$  behaviour and is caused by the entrainment process of turbulent air into the wake evolves downwind. In the case of no blade rotation and no wind veer (NV\_NR, region and the resulting wake recovery. The slightly smaller  $u$ -values in the bottom sector are related to the small increase of  $u_f$  over the rotor (Fig. 1(d)), no rotation of the flow occurs in the wake. 3(a).

If a stably stratified with a veering wind, described by an Ekman spiral characteristic of the Northern Hemisphere, interacts with clockwise rotating blades (V\_CCW), Comparing the sector averaged values of the EBL wind-turbine simulations (Fig. 13(a),

(c), (e) to the SBL wind-turbine simulations (Fig.13(b), (d), (f)), differences are especially pronounced in the CR case. Continuing with a comparison of the rotational direction of the flow in the near wake is opposite from the far wake (impact on wake characteristics under veering inflow, it shows striking differences for CR and CCR (Fig.13(b), (f)). The profiles of the  $v$ -sectors (Fig. 13(d)) are comparable to case B in the analysis chapter and the corresponding Fig. 4(a)-4(b). For a counterclockwise rotating rotor,  $v$  of the near wake is modified by  $v_v$ , gradually approaching  $v_f$  in the far wake. For a clockwise rotating rotor, the counterclockwise rotating flow results from clockwise rotating blades, whereas the strength of flow rotation mainly depends on  $\omega$  (Eqs. and ). This impact on the wake decreases with further distance downwind. In the far wake, wake rotation becomes smaller than the rotational direction component imposed on the flow by the veering wind. At that point, the rotational direction of the wake is determined by the flow and its veering wind as it is the case in the whole wake if a stably stratified with wind veer interacts with a non-rotating actuator. The change of the rotational direction of the flow in the wake in V\_CCW- $|v|$ -component, however, decreases in the near wake as seen in Fig. 6(i). In the lower rotor part, this decrease results from the superposition in Eq. 17 of the inflow from south to north, whereas the  $v_v$ -component is directed from north to south. Approaching downwind,  $|v|$  increases up to  $v = v_f$ . The upper rotor part is characterized by  $v_f < 0 \text{ m s}^{-1}$  (Fig. 4(a)) explains the different behaviour of flow recovery in the near wake and the far wake between V\_CCW- $v$ . Therefore,  $v$  of the top  $90^\circ$ -sector is only influenced by the positive  $v_v$ -component from south to north. Approaching downwind, the impact of  $v_v$  decreases, and  $v$  approaches  $v_f < 0$ . The non-symmetric behaviour of the bottom and top sectors in Fig. 4(a) and V\_NR-13(d) are related to the skewed wake in the lower rotor part in Fig. 4(e) and is also responsible for the smaller wake deflection angle in V\_CCW-7(b). Due to the wake deflection,  $v$  approaches  $v_f$  at a much smaller downwind distance in comparison to V\_NR (Fig. 4(a) vs. (e) and Fig. 4(a) vs. (e) the non-deflected upper rotor part (Figs. 9(b), 10(b)).

Considering the same stably stratified with a veering wind, where the same Ekman spiral interacts with counterclockwise rotating blades (V\_CW), the flow in the near wake consequently rotates in a clockwise direction (Due to the relatively large direction shear of  $0.25^\circ \text{ m}^{-1}$  in the lower rotor part and a moderate rotational frequency  $\Omega$  of  $0.117 \text{ s}^{-1}$ , the  $v$ -component in the lower rotor part decreases in CR in Fig. 4(e)). This rotational direction of the flow persists in the whole wake, as the rotational direction imposed by 13(d). However, the also results in a clockwise flow rotation in the far wake, where it becomes larger than the rotational direction component imposed on the flow by blade rotation. The resulting different rotational directions of the flow in the near wake in V\_CW and V\_CCW (sign did not change as predicted by Fig. 4(b). We would expect the change to occur for a fast enough rotation of the blades. In fact, the sign change does occur for a doubling of the rotational frequency of the SBL CR wind-turbine simulation (not shown).

The downwind evolution of  $w$  in Fig. 4(e) vs. (a)) explain the differences in the flow recovery 13(f) agrees with Eq. (10). The values of the northern and southern sectors differ, and for a clockwise rotating rotor,  $w > 0 \text{ m s}^{-1}$  in the southern sector (red solid line), whereas  $w < 0 \text{ m s}^{-1}$  in case of a counterclockwise rotating rotor (blue solid line) (Fig. 4(e) vs. (a)), in the spanwise wake width (6(m) - (p)). The  $u$ -values in Fig. 4(e) vs. 13(b) show the rotational direction dependence from Figs. 11(a)), and in the wake deflection angle (- (d) and 12(a) - (h), which is much more pronounced in the top sector of Fig. 4(e) vs. (a) and 13(b). The values of  $u$  are larger for CCR at each downwind position of the wake in the top sector. This larger difference between CR

and CCR in the top sector (Fig. ??(e)vs.13(b)) is somewhat surprising as the veering inflow is limited to the lower rotor part in Fig. 3(a).

Consequently, the rotational direction of the flow in the near wake is determined by the rotational direction of the wind turbine, whereas the rotational direction of the flow in the far wake is determined by the ambient wind veer, often dictated by the direction of the Ekman spiral and thus by the sign of the Coriolis force and the hemisphere. If the rotational directions of the flow in the near wake and the boundary layer flow intensify each other, the same rotational direction persists in the whole wake, as it is rotor (Fig. 2). Due to the veered inflow in the lower rotor part, the wake is deflected out of the considered sector region roughly at  $x = 3 D$  (Fig. 10(b), (f)). At  $x > 10 D$ , the case for a counterclockwise rotating wind turbine (V\_CW). Otherwise, the rotational direction of the flow will change in the wake as for a clockwise rotating wind turbine under veered inflow conditions at night in the Northern Hemisphere (V\_CCW). The position of the change of rotational direction,  $x_{fad}$ , depends on the strength of rotational direction imposed by the blades ( $\Omega$ ) and likewise on the strength of the veering wind, with a smaller rotational speed or a larger wind veer resulting in a smaller  $x_{fad}$ .  $u$ -values of the top sector become larger than the bottom sector ones (not shown), related to the significant increase of  $u_f$  with height over the rotor part (Fig. 3(a)).

## 6 Conclusions

To investigate the interaction of a veering wind with the rotational direction of a wind turbine in the wake in a stably stratified atmospheric boundary layer, we carry out a series of six LESs varying the incoming wind condition and both the magnitude and direction of the wind turbine rotation by applying incoming wind conditions from a non-veering EBL and a veering SBL extracted from a diurnal cycle simulation. The flow structures of the wake in the LESs are controlled by the rotational direction of the wind-turbine wake imposed by the blades (clockwise (CWCR) vs. counterclockwise (CCWCCR) vs. no rotation (NR)) and the inflow wind profiles (wind veer (V) vs. no wind veer (NV) EBL with no wind veer vs. SBL with veering wind).

The rotational direction of a wind turbine rotor in a stably stratified an EBL without wind veer only exerts a minor influence on the wake behaviour, which is limited to the near wake. This minor impact is consistent with previous investigations by Vermeer et al. (2003), Shen et al. (2007), Sande (2009), Kumar et al. (2013), Hu et al. (2013), Yuan et al. (2014), and Mühle et al. (2017).

In the presence of wind veer in an SBL, the rotational direction of a wind turbine, however, clearly impacts the streamwise elongation of the wake, the spanwise wake width, its spanwise width, the velocity deficit in the near wake, and the wake deflection angle. Wind veer. As the operating characteristics of upwind turbines, like their yaw with incoming flow, are already being adjusted to mitigate downwind impacts of wakes (Fleming et al., 2019), this work suggests that considering the direction of rotation could have benefits as well.

A veering wind occurs in a stably stratified SBL as long as the flow is not channelled. Veer reflects the change of vertical changes in interactions between the Coriolis force and friction with height in the absence of convective buoyancy, and



therefore happens convection. Veer occurs on many nights both onshore (Walter et al., 2009; Rhodes and Lundquist, 2013) and offshore (Bodini et al., 2019b) (Walter et al., 2009; Rhodes and Lundquist, 2013; Sanchez Gomez and Lundquist, 2020) and offshore (Bodini et al., 2019a, b). According to two years of meteorological tower measurements in Lubbock (Texas) (Walter et al., 2009), a stably stratified an SBL occurs in 52% of the measurements. A wind veer of 0.08 Veering (of some degree) occurs in well over 70% of those SBL occurrences ( $\approx 76\%$  in Walter et al. (2009) and  $\approx 78\%$  in Sanchez Gomez and Lundquist (2020)). In this work, we apply a directional shear between 10 m and 115 m of  $0.28^\circ \text{ m}^{-1}$ , as applied in this paper, corresponds to a frequency of occurrence of  $\approx 50\%$  of the measured veering wind situations. Therefore, considering a wind turbine operating at Lubbock (Texas) would spend half of its nighttime experience under veering wind conditions similar to this study. Given the significant impact, the choice of rotational direction of wind turbine blades in the Northern Hemisphere becomes critical.

similar to what would be calculated based on standard values for the Ekman spiral in the atmosphere. This very large directional shear occurs only in a minority of considered nights of roughly 1% in Walter et al. (2009, Fig. 3). Based on three months of lidar observations in north-central Iowa in Sanchez Gomez and Lundquist (2020, Fig. 7), a directional shear between 40 m and 120 m of  $0.25^\circ \text{ m}^{-1}$ , as it is the case in our SBL regime, occurs in 2% of the measurements. Comparing with 13 months of lidar observations off the coast of Massachusetts in Bodini et al. (2019a, Fig. 5), this very high wind veer occurs in 2% of the nights during summer and in 1% during winter. So in this study, to understand the possible significance of veer, we have explore a case with very strong veer.

The In the majority of the cases with veering inflow, the directional shear has lower values in comparison to the SBL wind-turbine simulations presented in this work. For example, a direction shear of  $\approx 0.08^\circ \text{ m}^{-1}$  occurs in 50% of the nights with veering wind in Walter et al. (2009). And yet, this work emphasizes the role of the interaction between inflow veer and wake rotation. When veer is present but smaller, we see an increasing impact of the rotational direction of a wind-turbine rotor on the wake characteristics can be explained by the linear superposition of rotor-induced vorticity with the veering wind. A simplified wake model of a wind turbine including a Rankine Vortex and the vertically sheared and veered boundary-layer flow can explain major features of this interaction. If the main parameters (wind speed, amount of veer over the rotor, rotational frequency of the wind turbine), necessary for the simplified wake model, are known for a specific wind-turbine site, this simple model could give instantaneously a first impression about the flow fields of  $v$  and  $w$  structure, being aware that this is a nonlinear process approaching towards the non-veered situation if the directional shear approaches  $0^\circ \text{ m}^{-1}$ . Therefore, in the majority of the nights with veering inflow in Walter et al. (2009), Bodini et al. (2019a), and Sanchez Gomez and Lundquist (2020), the prevailing directional shear would have a larger impact on the meridional flow in the wake. It could further represent the effect of a co-rotating wind turbine on its wake and consequently on the flow field encountered by a downwind turbine. As the operating characteristics of upwind turbines, like their yaw with incoming flow, are already being adjusted to mitigate downwind impacts of wakes (Fleming et al., 2019), this work suggests that considering the direction of rotation could have benefits as well. wake  $v$  as in the case considered in this work (if the rotational velocity of the blades has not changed). Smaller veer would not only lead to a stronger reduction of  $v$  for a clockwise rotating rotor, but also to a reversal for small enough values of the directional shear. In the majority of the cases in these measurement campaigns, the wake difference between clockwise



and counterclockwise rotating turbines would therefore be larger. Given the significant impact, the choice of rotational direction of wind-turbine blades in the Northern Hemisphere becomes more consequential.

5 ~~These~~ Our simulations represent a canonical case, and so real-world conditions may modify results. The veering wind simulated here is characteristic of a cloud free, nocturnal boundary-layer flow in the Northern Hemisphere. As the Coriolis force and the resulting Ekman spiral reverse direction in the Southern Hemisphere, the same effect should be prevalent in the Southern Hemisphere, however, with a ~~change of wake rotation at  $x_{Tad}$~~  reduction or reversion of the meridional wake component for counterclockwise rotating blades instead of clockwise rotating ones as it is the case in the Northern Hemisphere. Further, canonical Ekman spirals do not occur in every stably stratified ABL: conditions like cold air advection lead to a backing wind (Holton, 1973; Wallace and Hobbs, 2006), which is a wind that rotates in the counterclockwise direction with increasing height in the Northern Hemisphere. A backing wind ~~on~~ in the Northern Hemisphere interacting with both rotational directions will result in a different impact on the wake in comparison to a veering wind on the Northern Hemisphere, ~~and~~. It should be comparable to the Southern Hemispheric situation described above. Further, the evolution of the stable boundary layer through the evening transition ~~will lead to veer profiles other than the linear profile shown here (Rhodes and Lundquist, 2013; Lee and Lundquist, 2017; Englberger and Dörnbrack, 2018a)~~ can lead to a variety of veer profiles, in which the veering inflow is limited to the lower rotor half (Rhodes and Lundquist, 2013; Lee and Lundquist, 2017) or expands over the whole rotor (Abkar and Porté-Agel, 2016; Bromm et al., 2017; Churchfield and Sirnivas, 2018). But given the widespread occurrence of veer as noted by observational campaigns (~~Walter et al., 2009; Bodini et al., 2019b; Gomez and Lundquist, 20~~ Walter et al., 2009; Bodini et al., 2019b; Sanchez Gomez and Lundquist, 2020), as well as the interest in modifying wakes via active control of upwind turbines (Fleming et al., 2019), the work presented here can motivate further consideration of how inflow veer interacts with wind-turbine operations to affect downwind turbines.

*Author contributions.* All authors designed the idea. A. Englberger performed the simulations and prepared the manuscript with significant contributions from both co-authors.

*Competing interests.* The authors declare that they have no conflict of interest.

25 *Acknowledgements.* The authors gratefully acknowledge the Gauss Centre for Supercomputing e.V. (www.gauss-centre.eu) for funding this project by providing computing time on the GCS Supercomputer SuperMUC at Leibniz Supercomputing Centre (LRZ, www.lrz.de). This work was authored [in part] by the National Renewable Energy Laboratory, operated by Alliance for Sustainable Energy, LLC, for the U.S. Department of Energy (DOE) under Contract No. DE-AC36-08GO28308. Funding provided by the U.S. Department of Energy Office of Energy Efficiency and Renewable Energy Wind Energy Technologies Office. The views expressed in the article do not necessarily represent the views of the DOE or the U.S. Government. The U.S. Government retains and the publisher, by accepting the article for publication,

acknowledges that the U.S. Government retains a nonexclusive, paid-up, irrevocable, worldwide license to publish or reproduce the published form of this work, or allow others to do so, for U.S. Government purposes.

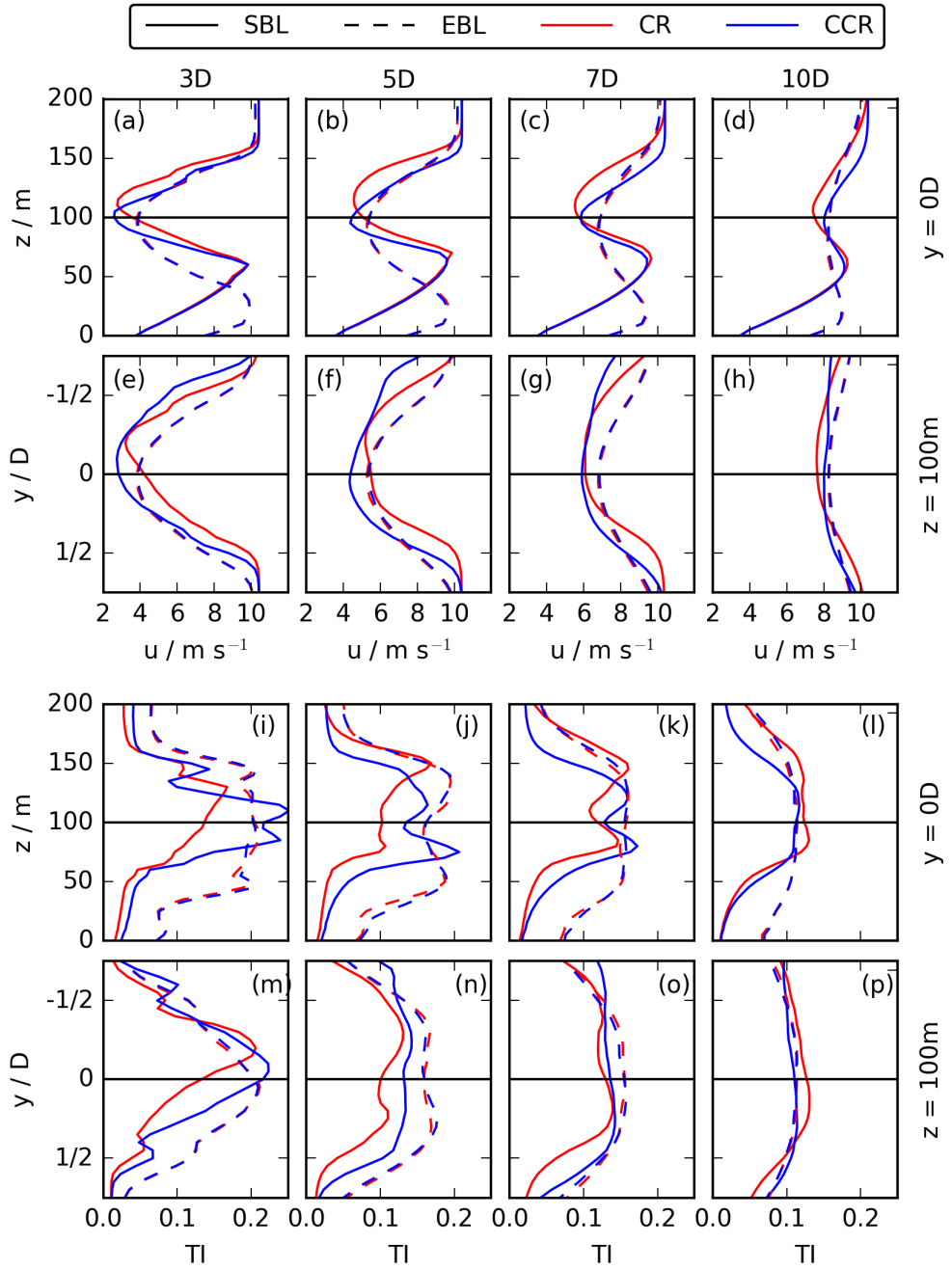
## References

- Abkar, M. and Porté-Agel, F.: The effect of atmospheric stability on wind-turbine wakes: A large-eddy simulation study, in: *Journal of Physics: Conference Series*, vol. 524, p. 012138, IOP Publishing, <https://doi.org/10.1088/1742-6596/524/1/012138>, 2014.
- Abkar, M. and Porté-Agel, F.: Influence of the Coriolis force on the structure and evolution of wind turbine wakes, *Physical Review Fluids*, 1, 063 701, <https://doi.org/10.1103/PhysRevFluids.1.063701>, 2016.
- Abkar, M., Sharifi, A., and Porté-Agel, F.: Wake flow in a wind farm during a diurnal cycle, *Journal of Turbulence*, 17, 420–441, <https://doi.org/10.1080/14685248.2015.1127379>, 2016.
- Aitken, M. L., Kosović, B., Mirocha, J. D., and Lundquist, J. K.: Large eddy simulation of wind turbine wake dynamics in the stable boundary layer using the Weather Research and Forecasting Model, *J Renew Sust Energy*, 6, 1529–1539, <https://doi.org/10.1063/1.4885111>, 2014.
- 10 Bak, C., Zahle, F., Bitsche, R., Kim, T., Yde, A., Henriksen, L. C., Hansen, M. H., Blasques, J. P. A. A., Gaunaa, M., and Natarajan, A.: The DTU 10-MW reference wind turbine, in: *Danish Wind Power Research 2013*, 2013.
- Bhaganagar, K. and Debnath, M.: Implications of Stably Stratified Atmospheric Boundary Layer Turbulence on the Near-Wake Structure of Wind Turbines, *Energies*, 7, 5740–5763, <https://doi.org/10.3390/en7095740>, 2014.
- Bhaganagar, K. and Debnath, M.: The effects of mean atmospheric forcings of the stable atmospheric boundary layer on wind turbine wake, *Journal of Renewable and Sustainable Energy*, 7, 013 124, <https://doi.org/10.1063/1.4907687>, 2015.
- 15 Bodini, N., Zardi, D., and Lundquist, J. K.: Three-dimensional structure of wind turbine wakes as measured by scanning lidar, *Atmospheric Measurement Techniques*, 10, 2017.
- Bodini, N., Lundquist, J. K., and Kirincich, A.: Offshore Wind Turbines will encounter very low Atmospheric Turbulence, arXiv preprint arXiv:1903.00080, 2019a.
- 20 Bodini, N., Lundquist, J. K., and Kirincich, A.: US East Coast Lidar Measurements Show Offshore Wind Turbines Will Encounter Very Low Atmospheric Turbulence, *Geophysical Research Letters*, 46, 5582–5591, <https://doi.org/10.1029/2019GL082636>, 2019b.
- Bromm, M., Vollmer, L., and Kühn, M.: Numerical investigation of wind turbine wake development in directionally sheared inflow, *Wind Energy*, 20, 381–395, 2017.
- Churchfield, M. J. and Sirmivas, S.: On the effects of wind turbine wake skew caused by wind veer, in: *2018 wind energy symposium*, p. 0755, 2018.
- 25 Dörenkämper, M., Witha, B., Steinfeld, G., Heinemann, D., and Kühn, M.: The impact of stable atmospheric boundary layers on wind-turbine wakes within offshore wind farms, *Journal of Wind Engineering and Industrial Aerodynamics*, 144, 146–153, <https://doi.org/10.1016/j.jweia.2014.12.011>, 2015.
- Englberger, A. and Dörnbrack, A.: Impact of Neutral Boundary-Layer Turbulence on Wind-Turbine Wakes: A Numerical Modelling Study, *Boundary-Layer Meteorology*, 162, 427–449, <https://doi.org/10.1007/s10546-016-0208-z>, 2017.
- 30 Englberger, A. and Dörnbrack, A.: Impact of the diurnal cycle of the atmospheric boundary layer on wind-turbine wakes: a numerical modelling study, *Boundary-layer meteorology*, 166, 423–448, <https://doi.org/10.1007/s10546-017-0309-3>, 2018a.
- Englberger, A. and Dörnbrack, A.: A Numerically Efficient Parametrization of Turbulent Wind-Turbine Flows for Different Thermal Stratifications, *Boundary-layer meteorology*, 169, 505–536, <https://doi.org/10.1007/s10546-018-0377-z>, 2018b.
- 35 Englberger, A. and Dörnbrack, A.: Wind-turbine wakes responding to stably stratified flow over complex terrain, in: *Journal of Physics: Conference Series*, vol. 1037, p. 072014, IOP Publishing, <https://doi.org/10.1088/1742-6596/1037/7/072014>, 2018c.

- Fleming, P., King, J., Dykes, K., Simley, E., Roadman, J., Scholbrock, A., Murphy, P., Lundquist, J. K., Moriarty, P., Fleming, K., et al.: Initial results from a field campaign of wake steering applied at a commercial wind farm—Part 1, *Wind Energy Science*, 4, 273–285, <https://doi.org/10.5194/wes-4-273-2019>, 2019.
- Fröhlich, J.: *Large Eddy Simulation turbulenter Strömungen*, Teubner Verlag / GWV Fachverlage GmbH, Wiesbaden, 414 pp, 2006.
- 5 Gomez, M. S. and Lundquist, J.: The Effects of Wind Veer During the Morning and Evening Transitions, in: *Journal of Physics: Conference Series*, vol. 1452, p. 012075, 2020.
- Heimann, D., Käsler, Y., and Gross, G.: The wake of a wind turbine and its influence on sound propagation, *Meteorol Z*, 20, 449–460, <https://doi.org/10.1127/0941-2948/2011/0273>, 2011.
- Holton, J. R.: An introduction to dynamic meteorology, *American Journal of Physics*, 41, 752–754, 1973.
- 10 Hu, H., Yuan, W., Ozbay, A., and Tian, W.: An experimental investigation on the effects of turbine rotation directions on the wake interference of wind turbines, in: *51st AIAA Aerospace Sciences Meeting including the New Horizons Forum and Aerospace Exposition*, p. 607, 2013.
- Jungo, G. V., Wu, Y.-T., and Porté-Agel, F.: Field measurements of wind turbine wakes with lidars, *J Atmos Ocean Technol*, 30, 274–287, 2013.
- Kapoor, A., Ouakka, S., Arwade, S. R., Lundquist, J., Lackner, M. A., Myers, A. T., Worsnop, R. P., and Bryan, G. H.: Hurricane eyewall  
15 winds and structural response of wind turbines, Tech. rep., National Renewable Energy Lab.(NREL), Golden, CO (United States), 2019.
- Kataoka, H. and Mizuno, M.: Numerical flow computation around aeroelastic 3D square cylinder using inflow turbulence, *Wind and Structures*, 5, 379–392, 2002.
- Kühnlein, C., Smolarkiewicz, P. K., and Dörnbrack, A.: Modelling atmospheric flows with adaptive moving meshes, *J Comput Phys*, 231, 2741–2763, <https://doi.org/10.1016/j.jcp.2011.12.012>, 2012.
- 20 Kumar, P. S., Abraham, A., Bensingh, R. J., and Ilangovan, S.: Computational and experimental analysis of a counter-rotating wind turbine system, 2013.
- Lamb, H.: *Hydrodynamics*, Cambridge university press, 1993.
- Lee, J. C. and Lundquist, J. K.: Observing and Simulating Wind-Turbine Wakes During the Evening Transition, *Boundary-Layer Meteorology*, 164, 449–474, <https://doi.org/10.1007/s10546-017-0257-y>, 2017.
- 25 Maegaard, P., Krenz, A., and Palz, W.: *Wind power for the world: the rise of modern wind energy*, Jenny Stanford, 2013.
- Margolin, L. G., Smolarkiewicz, P. K., and Sorbjan, Z.: Large-eddy simulations of convective boundary layers using nonoscillatory differencing, *Phys D Nonlin Phenom*, 133, 390–397, [https://doi.org/10.1016/S0167-2789\(99\)00083-4](https://doi.org/10.1016/S0167-2789(99)00083-4), 1999.
- Mirocha, J. D., Kosović, B., Aitken, M. L., and Lundquist, J. K.: Implementation of a generalized actuator disk wind turbine model into the weather research and forecasting model for large-eddy simulation applications, *J Renew Sust Energy*, 6, 013 104,  
30 <https://doi.org/10.1063/1.4861061>, 2014.
- Mühle, F., Adaramola, M. S., and Sætran, L.: The effect of rotational direction on the wake of a wind turbine rotor—a comparison study of aligned co-and counter rotating turbine arrays, *Energy Procedia*, 137, 238–245, <https://doi.org/10.1016/j.egypro.2017.10.346>, 2017.
- Naughton, J. W., Heinz, S., Balas, M., Kelly, R., Gopalan, H., Lindberg, W., Gundling, C., Rai, R., Sitaraman, J., and Singh, M.: Turbulence and the isolated wind turbine, in: *6th AIAA Theoretical Fluid Mechanics Conference*, pp. 1–19., Honolulu, Hawaii, 2011.
- 35 Prusa, J. M., Smolarkiewicz, P. K., and Wyszogrodzki, A. A.: EULAG, a computational model for multiscale flows, *Computers & Fluids*, 37, 1193–1207, <https://doi.org/10.1016/j.compfluid.2007.12.001>, 2008.
- Rhodes, M. E. and Lundquist, J. K.: The effect of wind-turbine wakes on summertime US Midwest atmospheric wind profiles as observed with ground-based doppler lidar, *Boundary-Layer Meteorol*, 149, 85–103, <https://doi.org/10.1007/s10546-013-9834-x>, 2013.

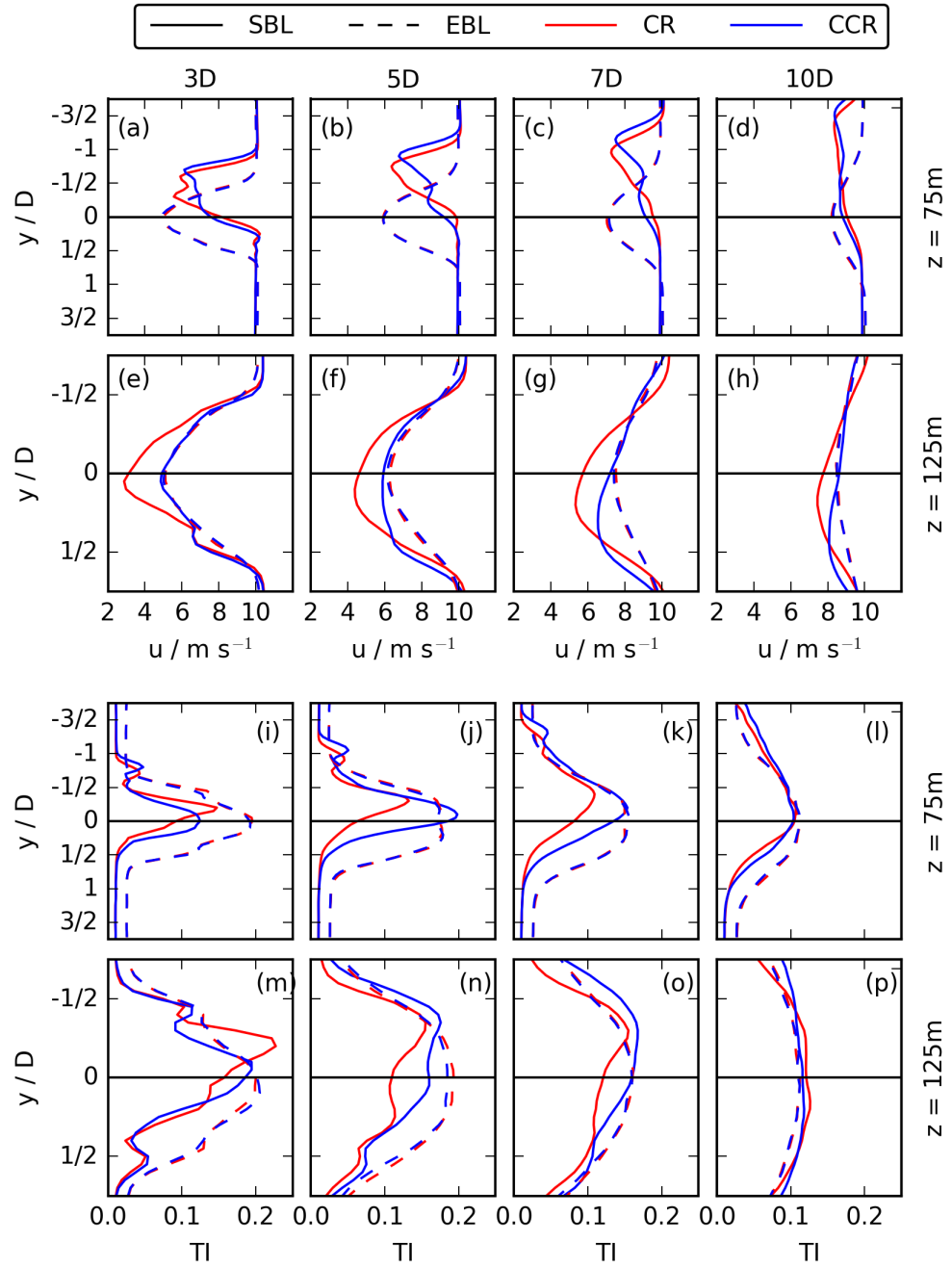
- Sanchez Gomez, M. and Lundquist, J. K.: The effect of wind direction shear on turbine performance in a wind farm in central Iowa, *Wind Energy Science (Online)*, 5, 2020.
- Sanderse, B.: Aerodynamics of wind turbine wakes, Energy Research Center of the Netherlands (ECN), ECN-E-09-016, Petten, The Netherlands, Tech. Rep, 5, 153, 2009.
- 5 Schmidt, H. and Schumann, U.: Coherent structure of the convective boundary layer derived from large-eddy simulations, *J Fluid Mech*, 200, 511–562, <https://doi.org/10.1017/S0022112089000753>, 1989.
- Shapiro, A. and Fedorovich, E.: Analytical description of a nocturnal low-level jet, *Quarterly Journal of the Royal Meteorological Society*, 136, 1255–1262, 2010.
- Shen, W. Z., Zakkam, V. A. K., Sørensen, J. N., and Appa, K.: Analysis of counter-rotating wind turbines, in: *Journal of Physics: Conference Series*, vol. 75, p. 012003, IOP Publishing, <https://doi.org/10.1088/1742-6596/75/1/012003>, 2007.
- 10 Smolarkiewicz, P. K. and Margolin, L. G.: On forward-in-time differencing for fluids: extension to a curvilinear framework, *Mon Weather Rev*, 121, 1847–1859, [https://doi.org/10.1175/1520-0493\(1993\)121<1847:OFITDF>2.0.CO;2](https://doi.org/10.1175/1520-0493(1993)121<1847:OFITDF>2.0.CO;2), 1993.
- Smolarkiewicz, P. K. and Margolin, L. G.: MPDATA: A Finite-Difference Solver for Geophysical Flows, *J Comput Phys*, 140, 459–480, <https://doi.org/10.1006/jcph.1998.5901>, 1998.
- 15 Smolarkiewicz, P. K. and Prusa, J. M.: Towards mesh adaptivity for geophysical turbulence: continuous mapping approach, *Int J Numer Meth Fl*, 47, 789–801, <https://doi.org/10.1002/flid.858>, 2005.
- Smolarkiewicz, P. K. and Pudykiewicz, J. A.: A class of semi-Lagrangian approximations for fluids, *J Atmos Sci*, 49, 2082–2096, [https://doi.org/10.1175/1520-0469\(1992\)049<2082:ACOSLA>2.0.CO;2](https://doi.org/10.1175/1520-0469(1992)049<2082:ACOSLA>2.0.CO;2), 1992.
- Smolarkiewicz, P. K. and Winter, C. L.: Pores resolving simulation of Darcy flows, *J Comput Phys*, 229, 3121–3133, <https://doi.org/10.1016/j.jcp.2009.12.031>, 2010.
- 20 Smolarkiewicz, P. K., Sharman, R., Weil, J., Perry, S. G., Heist, D., and Bowker, G.: Building resolving large-eddy simulations and comparison with wind tunnel experiments, *J Comput Phys*, 227, 633–653, <https://doi.org/10.1016/j.jcp.2007.08.005>, 2007.
- Stull, R. B.: *An Introduction of Boundary Layer Meteorology*, Dordrecht, Kluwer Academic, 1988.
- Vermeer, L., Sørensen, J. N., and Crespo, A.: Wind turbine wake aerodynamics, *Progress in aerospace sciences*, 39, 467–510, [https://doi.org/10.1016/S0376-0421\(03\)00078-2](https://doi.org/10.1016/S0376-0421(03)00078-2), 2003.
- 25 Vollmer, L., Lee, J. C., Steinfeld, G., and Lundquist, J.: A wind turbine wake in changing atmospheric conditions: LES and lidar measurements, in: *Journal of Physics: Conference Series*, vol. 854, p. 012050, IOP Publishing, <https://doi.org/10.1088/1742-6596/75/1/012003>, 2017.
- Wallace, J. M. and Hobbs, P. V.: *Atmospheric science: an introductory survey*, vol. 92, Elsevier, 2006.
- 30 Walter, K., Weiss, C. C., Swift, A. H., Chapman, J., and Kelley, N. D.: Speed and direction shear in the stable nocturnal boundary layer, *Journal of Solar Energy Engineering*, 131, 011 013, <https://doi.org/10.1115/1.3035818>, 2009.
- Wedi, N. P. and Smolarkiewicz, P. K.: Extending Gal-Chen and Somerville terrain-following coordinate transformation on time-dependent curvilinear boundaries, *J Comput Phys*, 193, 1–20, <https://doi.org/10.1016/j.jcp.2003.07.034>, 2004.
- Witha, B., Steinfeld, G., and Heinemann, D.: High-resolution offshore wake simulations with the LES model PALM, in: *Wind energy - Impact of turbulence*, pp. 175–181., Spring 2012, Oldenburg, Germany, 2014.
- 35 Yamada, T. and Mellor, G.: A simulation of the Wangara atmospheric boundary layer data, *Journal of the Atmospheric sciences*, 32, 2309–2329, 1975.

- Yuan, W., Tian, W., Ozbay, A., and Hu, H.: An experimental study on the effects of relative rotation direction on the wake interferences among tandem wind turbines, *Science China Physics, Mechanics & Astronomy*, 57, 935–949, 2014.
- Zhang, W., Markfort, C. D., and Porté-Agel, F.: Near-wake flow structure downwind of a wind turbine in a turbulent boundary layer, *Exp Fluids*, 52, 1219–1235, <https://doi.org/10.1007/s00348-011-1250-8>, 2012.



Flow-rotation-of- $v$

**Figure 11.** Vertical and  $w$  at 3D spanwise profiles of  $u$  (first row), 5D (second row two rows), and 7D-TI (third row last two rows) behind through the disc center of the rotor at  $y = 0D$  and  $z = 100m$  for V-CCW the SBL and the EBL wind-turbine simulations at  $x = 3D$  (left first column), V-NR 5D (middle second column), 7D (third column), and V-CW 10D (right fourth column). The red dot marks the rotor centre downwind and the blue contour the rotor region for both rotational directions CR and CCR.



Flow-rotation

**Figure 12.** Spanwise profiles of  $v$  and  $w$  at  $3D$   $u$  (first row two rows),  $5D$  and  $TI$  (second row last two rows), at  $z = 75$  m in the first and  $7D$  (third row) behind and at  $z = 125$  m in the disc second and last row for NV-CCW the SBL and the EBL wind-turbine simulations at  $x = 3D$  (left first column), NV-NR-5D (middle second column), 7D (third column), and NV-CW-10D (right fourth column). The red dot marks the rotor center downwind and the blue contour the rotor region for both rotational directions CR and CCR.



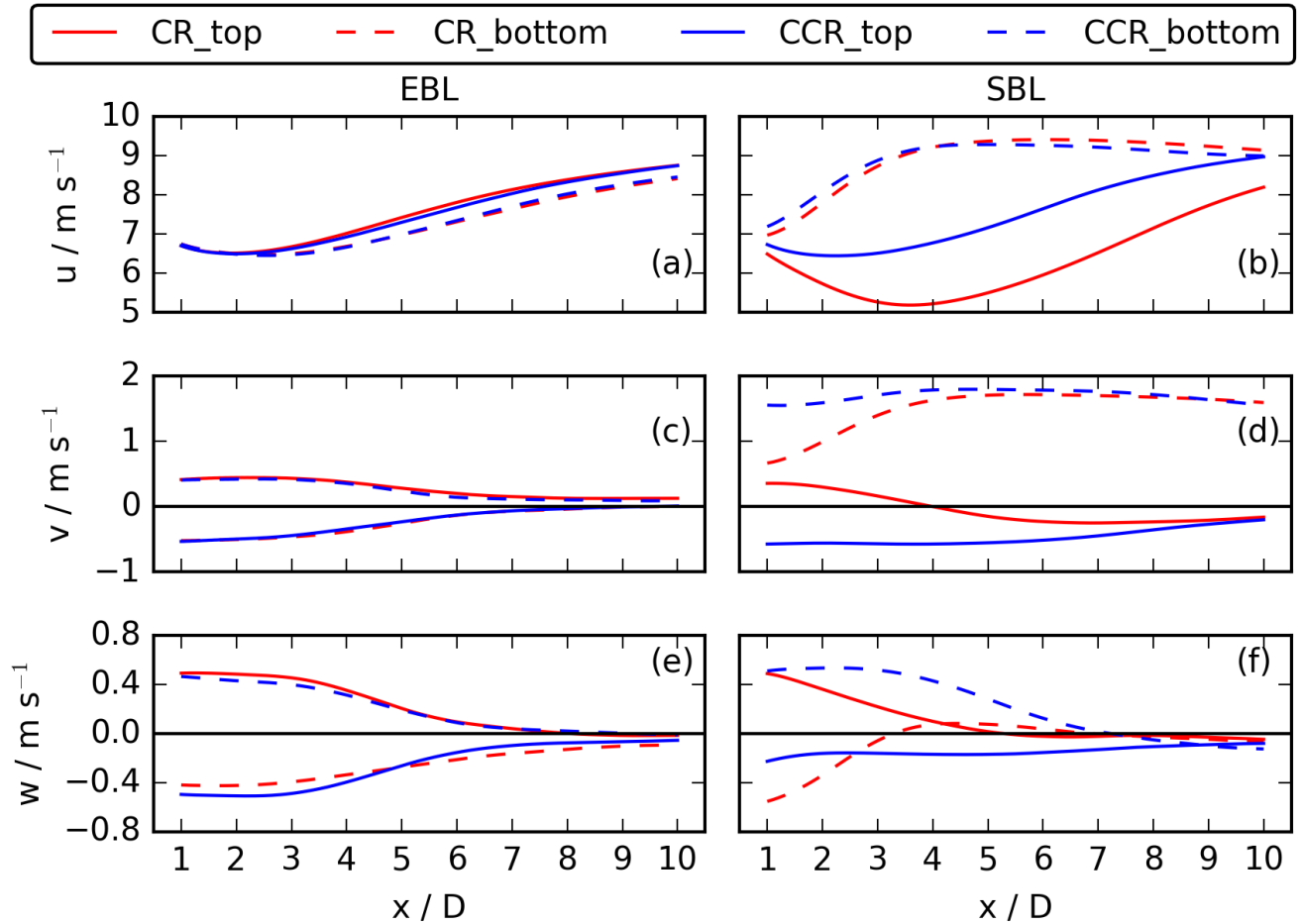


**Figure 13.** Sector and time averages of  $u$ ,  $v$ , and  $w$  for the EBL wind-turbine simulations (first column) and the SBL wind-turbine simulations (second column).  $u$  and  $v$  show the top and bottom  $90^\circ$ -sectors,  $w$  the southern (solid line) and northern (dashed line) sectors.